

**CHARGE-INDUCED ACTUATION OF TWO-DIMENSIONAL (2D)
NIOBIUM BASED TRANSITION-METAL DICHALCOGENIDES: A
FIRST-PRINCIPLES STUDY**

ELTON MAH SONG ZHE


**A project report submitted in partial fulfilment of the
requirements for the award of Bachelor of Science
(Honours) Physics**

**Lee Kong Chian Faculty of Engineering and Science
Universiti Tunku Abdul Rahman**

January 2022

DECLARATION

I hereby declare that this project report is based on my original work except for citations and quotations which have been duly acknowledged. I also declare that it has not been previously and concurrently submitted for any other degree or award at UTAR or other institutions.

Signature : 
Name : ELTON MAH SONG ZHE
ID No. : 1900237
Date : 12/9/2022

APPROVAL FOR SUBMISSION

I certify that this project report entitled “**CHARGE-INDUCED ACTUATION OF TWO-DIMENSIONAL (2D) NIOBIUM BASED TRANSITION-METAL DICHALCOGENIDES: A FIRST-PRINCIPLES STUDY**” was prepared by **ELTON MAH SONG ZHE** has met the required standard for submission in partial fulfilment of the requirements for the award of Bachelor of Science (Honours) Physics at Universiti Tunku Abdul Rahman.

Approved by,

Signature

:



Supervisor

:

YE OH KEAT HOE

Date

:

28/9/2022

The copyright of this report belongs to the author under the terms of the copyright Act 1987 as qualified by Intellectual Property Policy of Universiti Tunku Abdul Rahman. Due acknowledgement shall always be made of the use of any material contained in, or derived from, this report.

© 2022, Elton Mah Song Zhe. All right reserved.

ACKNOWLEDGEMENTS

I would like to express my gratitude to my research supervisor, Dr. Yeoh Keat Hoe for his invaluable advice, guidance and his enormous patience throughout the development of the research. The completion of this project could not also be successful without the support of my peers and everyone who had contributed to this project.

In addition, I would also like to express my gratitude to my loving parents and friends who had helped and given me encouragement throughout my undergraduate study. Without their continuous support, I would never have been able to pursue my bachelor's degree up to completing my Final Year Project.

Furthermore, I would like to thank the forerunners in the field of Density Functional Theory, and scientists and mathematicians that continuously try to improve or utilize the theory that provide us a way to conduct study on materials within its framework.

Last but not least, I would like to express my gratitude to communities of Quantum ESPRESSO users that dedicate their time to provide guidance, tutorials and solutions to problems on forums and other platform alike.

ABSTARCT

Ever since the experimental realization of graphene, two-dimensional (2D) materials have been an attractive field of research and extensively studied. 2D materials have received excessive attention from the solid state and material science scientific communities due to their exceptional and interesting electronic and mechanical properties. In this project, first-principles calculations based on density-functional theory (DFT) are performed using the Quantum ESPRESSO package to investigate the charge-induced electromechanical properties of 2D transition metal dichalcogenides (TMDCs), namely Niobium Disulfide (NbS_2) and Niobium Diselenide (NbSe_2), alongside with XCrySDen to visualize the atomic structures. The calculations are carried out to analyze the actuation responses such as stress and strain generated by the 2D materials in the case of charge doping. These results provide an important insight into their excellent properties as electromechanical actuators, making them attractive candidates and useful for artificial muscle applications.

TABLE OF CONTENTS

ACKNOWLEDGEMENTS	v
ABSTRACT	vi
TABLE OF CONTENTS	viii
LIST OF TABLES	ixx
LIST OF FIGURES	x
LIST OF SYMBOLS / ABBREVIATIONS	xiii

CHAPTER

1	INTRODUCTION	1
	1.1 Introduction to Two-Dimensional (2D) Material	1
	1.2 Introduction to Transition Metal Dichalcogenides	3
	1.3 Problem Statement	4
	1.4 Aim and Objectives	5
	1.5 Scope and Limitation of the Study	6
2	THEORETICAL BACKGROUND	8
	2.1 Density Functional Theory (DFT)	8
	2.1.1 Many-Body System	8
	2.1.2 The Hohenberg-Kohn (HK) theorems	9
	2.1.3 The Kohn-Sham equations	10
	2.1.4 Born-Oppenheimer Approximation	12
	2.1.5 Band Structure	12
	2.1.6 Spin-Orbit Coupling	12
	2.1.7 Density of States (DOS)	13
	2.1.8 Exchange-Correlation (XC) Functional	13
	2.1.9 Bloch's Theorem	14
	2.1.10 Plane Wave	15
	2.2 Pseudopotential	16
	2.2.1 Norm-conserving pseudopotential	16
3	LITERATURE REVIEW	17
	3.1 Niobium Disulphide (NbS ₂)	17

	3.1.1 Structural Properties	17
	3.1.2 Electronic Properties	19
	3.1.3 Mechanical Properties	21
	3.2 Niobium Diselenide (NbSe ₂)	22
	3.2.1 Structural Properties	22
	3.2.2 Electronic Properties	24
	3.2.3 Mechanical Properties	25
4	METHODOLOGY AND WORK PLAN	27
	4.1 DFT calculation with Quantum ESPRESSO	27
	4.2 Visualization of crystal structure with XCrySDen	27
	4.3 Performing Calculations	29
	4.4 High Symmetry Point	30
	4.5 Work Plan	31
	4.5.1 Structural Optimization and Electronic Properties Calculation	31
	4.5.2 Calculation of Actuator Performance	31
	4.5.3 Calculation of Mechanical Properties	32
5	RESULTS AND DISCUSSIONS	35
	5.1 Niobium Disulphide (NbS ₂)	35
	5.1.1 Convergence Tests	36
	5.1.2 Band Structure and Density of States	37
	5.2 Niobium Diselenide (NbSe ₂)	38
	5.2.1 Convergence Tests	39
	5.2.2 Band Structure and Density of States	40
	5.3 Crystal Structure	41
	5.4 Actuator Performance	42
	5.5 Mechanical Performance	43
6	CONCLUSION AND RECOMMENDATION	47
	6.1 Summary	47
	6.2 Recommendation for Future Works	47
	6.3 Problems Encountered	48
	6.4 Recommended Solutions	48
	REFERENCES	49

LIST OF TABLES

Table 3.1: Some examples of different types of phases and packings in NbS ₂	18
Table 3.2: DFT calculated mechanical properties for NbS ₂ (Hao Sun et.al., 2021)	21
Table 3.3: Some examples of different types of phases and packings in NbSe ₂ (Sidoumou et al., 2021)	23
Table 3.4: DFT calculated mechanical properties for NbSe ₂ (Hao Sun et.al., 2021)	26
Table 5.1: Lattice constants of NbS ₂ from literature review that applied GGA functional	41
Table 5.2: Lattice constants of NbS ₂ from literature review that applied GGA functional	41
Table 5.3: Mechanical properties of neutral charge (q=0) NbS ₂ and NbSe ₂	43

LIST OF FIGURES

Figure 1.1: Atomic structures of some general 2D materials (Xuanye Leng et.al., 2021)	1
Figure 1.2: Atomic structures of TMDC MoS ₂ (Johnny Wong., 2014)	4
Figure 2.1: General steps to solve the DFT for self-consistency	10
Figure 2.2: Flow chart diagram for obtaining the Self-Consistent Field (SCF) calculation using Kohn-Sham equations	11
Figure 2.3: A graph of pseudopotential and its corresponding pseudo wavefunction	16
Figure 3.1: Crystal structure of NbS ₂ (Ossila)	17
Figure 3.2: Types of TMDCs crystal structure and phases where transition metal atoms are shown in blue and chalcogen atoms are shown in yellow (Kim & Lee, 2018)	18
Figure 3.3: Crystal structures of 2H- NbS ₂ (Tissen <i>et al.</i> , 2013)	19
Figure 3.4: Electronic Band Structure of 2H- NbS ₂ (Doran <i>et al.</i> , 2001)	19
Figure 3.5: Density of States (DOS) of 2H- NbS ₂ (Doran <i>et al.</i> , 2001)	20
Figure 3.6: Band structures of NbS ₂ under external strain ranging from -5% to 5% (Yanmei Zang, Yandong Ma, 2020)	20
Figure 3.7: Stress-strain curves of NbS ₂ highlighted in green (a) and (b) x uniaxial tension, (c) and (d) y-uniaxial, (e) and (f) biaxial along x and y directions respectively. (Hao Sun et.al., 2021)	22
Figure 3.8: Crystal structure of NbSe ₂ (Hong Wang <i>et al.</i> , 2017)	22
Figure 3.9: Crystal structure of 2H- NbSe ₂ (Sidoumou <i>et al.</i> , 2021)	23
Figure 3.10: Electronic Band Structure of 2H- NbSe ₂ (Doran <i>et al.</i> , 2001)	24
Figure 3.11: Density of States (DOS) of 2H- NbSe ₂ (Doran <i>et al.</i> , 2001)	24
Figure 3.12: Electronic band structures and DOS of the relaxed 2D NbSe ₂ (Yeoh <i>et al.</i> , 2020)	25
Figure 3.13: Band structures of NbSe ₂ under external strain ranging from -5%	

to 5% (Yanmei Zang, Yandong Ma, 2020)	25
Figure 3.14: Stress-strain curves of NbSe ₂ highlighted in blue (a) and (b) x- uniaxial tension, (c) and (d) y-uniaxial, (e) and (f) biaxial along x and y directions respectively	26
Figure 4.1: Quantum ESPRESSO. (Giannozzi, 2009)	27
Figure 4.2: XCrySDen's User Interface	28
Figure 4.3: Interface of Measuring the Atomic Distance using XCrySDen.	28
Figure 4.4: Input file for (a) SCF calculation and (b) Geometrical Relaxation via QE	29
Figure 4.5: Command to initiate the computation via Linux Terminal	29
Figure 4.6: Brillouin Zone for a Hexagonal System (Retrieved from Bilbao crystallographic server)	30
Figure 4.7: XCrySDen k-path selection	30
Figure 4.8: High Symmetry k-points	30
Figure 4.9: Flowchart of DFT calculation using Quantum Espresso for electronic and structural properties	31
Figure 4.10: Inserting a total charge of 0.12 into the input file	32
Figure 5.1: Top and Side view of NbS ₂ atomic structure from XCrySDen	35
Figure 5.2: Convergence calculation for the cut-off energy of NbS ₂	36
Figure 5.3: Convergence calculation for the k points grid of NbS ₂	37
Figure 5.4: The calculated band structure and DOS for NbS ₂	37
Figure 5.5: Top and Side view of NbSe ₂ atomic structure from XCrySDen	38
Figure 5.6: Convergence calculation for the cut-off energy of NbSe ₂	39
Figure 5.7: Convergence calculation for the k points grid of NbSe ₂	40
Figure 5.8: The calculated band structure and DOS for NbS ₂	40

Figure 5.9: Actuator strain of NbS ₂ as a function of charge doping ranging from -0.12 to 0.12 e per atom.	42
Figure 5.10: Actuator strain of NbSe ₂ as a function of charge doping ranging from -0.12 to 0.12 e per atom.	42
Table 5.11: The stress-strain curve of NbS ₂ in biaxial, x and y directions.	44
Table 5.12: The stress-strain curve of NbSe ₂ in biaxial, x and y directions.	44
Table 5.13: Young's moduli of NbS ₂ and NbSe ₂ plotted as function of charge doping per atom	45
Table 5.14: Stress generated by NbS ₂ and NbSe ₂ plotted as function of charge doping per atom	45
Table 5.15: Work density per cycle of NbS ₂ and NbSe ₂ plotted as function of charge doping per atom	46

LIST OF SYMBOLS / ABBREVIATIONS

2D	Two-Dimensional
TMDC	Transition Metal Dichalcogenides
DFT	Density Functional Theory
SCF	Self-Consistent Field
LDA	Local Density Approximation
GGA	Generalized Gradient Approximation
PBE	Perdew-Burke-Ernzerhof
PAW	Projected Augmented Wave
XC	Exchange-Correlation
DOS	Density of States
TDOS	Total Density of States
QE	Quantum Espresso
HK	Hohenberg-Kohn
KS	Kohn-Sham
Å	Angstrom, 10^{-10} meter
Ry	Rydberg, 13.6 eV
eV	Electron-volt
E_F	Fermi energy
E	Energy
NbS_2	Niobium Disulphide
$NbSe_2$	Niobium Diselenide
$n(r)$	Electron density at generalized coordinate r
\hat{H}	Hamiltonian Operator
∇^2	Laplacian Operator
ϕ	Wavefunction
$E[n(r)]$	Energy Functional
T	Kinetic Energy
V	Potential Energy

U	Electron-ion Interaction Energy
MoS_2	Molybdenum Disulfide
H	Hexagonal
T	Trigonal

CHAPTER 1

INTRODUCTION

1.1 Introduction to Two-Dimensional (2D) Material

Two-dimensional layered materials or 2D materials is defined as a family of crystalline materials comprise of only a single atom-thick layer, or in other words, a monolayer. The group of 2D materials are usually classified into either single element allotropes with the suffix “-ene” such as borophene or compounds of various elements with the suffixes “-ide” or “-ane”. Some examples of commonly known 2D materials are shown in Fig. 1.1 below.

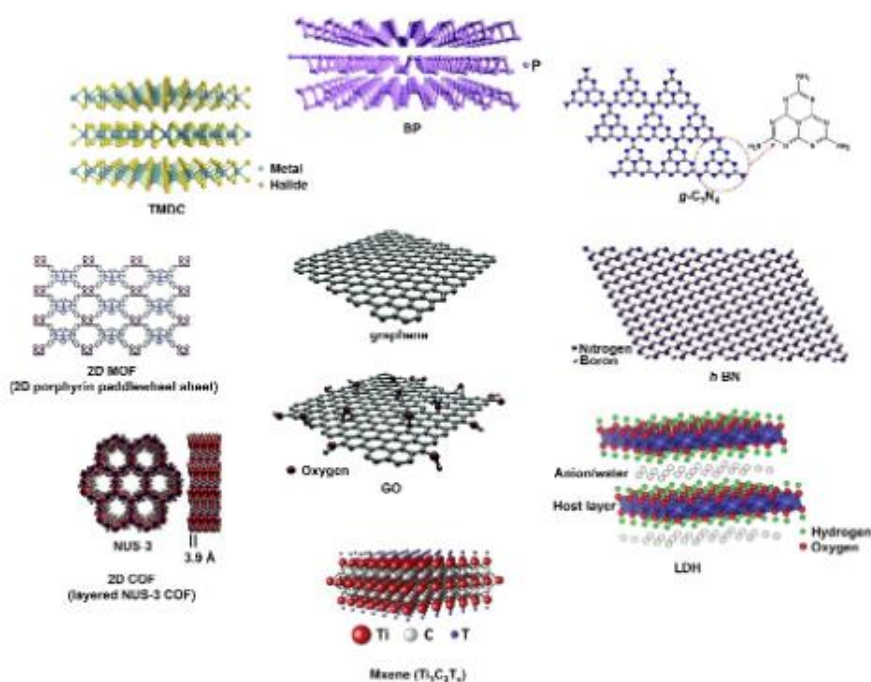


Figure 1.1: Atomic structures of some general 2D materials (Xuanye Leng et.al., 2021)

2D materials have been an attractive field of research and extensively studied ever since the experimental realization of graphene, a single atom layered graphite, by physicists Andre Geim and Konstantin Novoselov from University of Manchester, England back in 2004 (Novoselov et al., 2004). This first ever

2D material was discovered by simply exfoliating graphite, its bulk form, by using scotch tape, which this process is now known as mechanical exfoliation. From that day onwards, 2D materials have received excessive attention from the solid state and material science scientific communities due to their exceptional and interesting properties. Nowadays, the 2D materials family has already expanded beyond graphene. As shown in Fig. 1.1, these are some of schematic structures of 2D materials known to mankind; Hexagonal boron nitride (h-BN), graphene oxide (GO), transition-metal dichalcogenide (TMDC), 2D metal oxide, graphene, and 2D perovskite, just to name a few.

The 2D materials have been a promising material due to their unique properties. One of the many outstanding aspects of 2D materials is exhibiting high specific surface area. For example, the high specific surface area of graphene of approximately $2630 \text{ m}^2/\text{g}$ can be used as additives in supercapacitors (Xuanye Leng et.al., 2021). Moreover, graphene also has an electron mobility that is above $15,000 \text{ cm}^2\text{V}^{-1}\text{s}^{-1}$ which allow quantum Hall effect in room-temperature (Geim and Novoselov, 2009). The effective mass of electron in graphene of zero is in relation to the band structure of graphene where it forms 6 Dirac point at the vertices of its Brillouin Zone (BC). There are other exceptional properties for graphene as well: For instance, a Young's modulus of around 1 TPa, an intrinsic mobility of $200000 \text{ cm}^2\text{V}^{-1}\text{s}^{-1}$ at room temperature materials (Xuanye Leng et.al., 2021). Unfortunately, the only drawback to graphene is its limitation in the ability to turn off for semiconductor applications. They are many more intriguing properties of 2D materials where we will discuss further in detail.

2D materials are commonly mechanically exfoliated from its bulk form where monolayers are stacked and bonded by weak van der Waals between layer (Novoselov et al., 2005). Compared to their bulk counterparts, 2D materials not only have higher tensile strength and can withstand larger stress, but also exhibit direct band gap whereas when they are bonded by weak interlayer forces, they exhibit indirect band gap and can be easily displaced. The optoelectronic properties of 2D materials are also able to be modulated by straining and stretching the material. In these processes, the band gap can be shifted from

indirect to direct (Roldán *et al.*, 2015), their band structure, density of states (DOS), and charge density can also be altered. (Garay-Tapia, Romero and Barone, 2012).

With tolerable and rigid structures, extraordinary electronic properties, tuneable capability as well as superior conductivity, 2D materials have manifested optimistic potential in various fields such as optoelectronic devices, battery engineering and catalyst. However, as of writing this report, most of the applications are still constrained to laboratory scale. To obtain a commercially affordable and easily to fabricate 2D materials, the race to find one has been going on intensively ever since the sparked from graphene. Later in this report, Niobium-based transition-metal dichalcogenides has been selected as the subject of study for the next potential 2D material to replace silicon based electronic used today.

1.2 Introduction to Transition Metal Dichalcogenides

One of the most prominent types of material from the 2D family is the transition metal dichalcogenides (TMDCs). TMDC monolayers are compound monolayers in the form of MX_2 with M being a transition metal atom such as vanadium (V), niobium (Nb), molybdenum (Mo), titanium (Ti), tungsten (W) and others, combined with two X atoms of the chalcogen family, group 16 elements, such as selenium (Se), sulphur (S), tellurium (Te) and others. Some examples of TMDC are NbS_2 , VSe_2 , TaS_2 and MoS_2 . The interlayer force of TMDC monolayers is van-der-Waals attraction force, which is similar to that of graphene, so single atomic thick TMDC monolayers (which are slightly thicker than graphene) can also be exfoliated from their bulk form by mechanical or chemical means. TMDC has a range of conductivity, so they can be categorized into conductor, semimetal, semiconductor and insulator. This gives TMDC an advantage over graphene in electronics, optoelectronics, spintronics and semiconductors application. Among the TMDC materials, MoS_2 is the most commonly known 2D material studied for its exotic properties. As shown in Fig. 1.2 below, 1.79 eV of direct energy band gap is exhibited by MoS_2 .

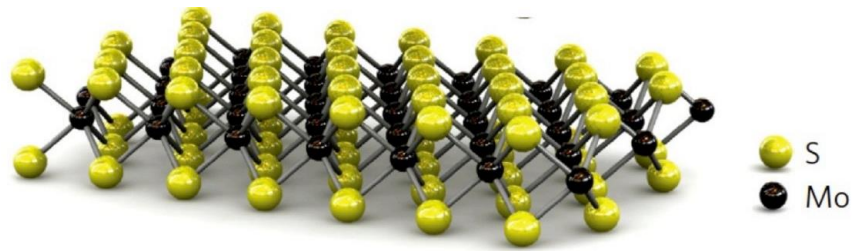


Figure 2.2: Atomic structures of TMDC MoS_2 (Johnny Wong., 2014)

In 2011, the first MoS_2 transistor with 0.65 nm channel thickness and mobility of at least $200 \text{ cm}^2\text{V}^{-1}\text{s}^{-1}$ which is comparable to that of graphene nanoribbons, was constructed (Radisavljevic et al., 2011). This achievement has demonstrated the potential of TMDC in flexible transistors, memory storage device, sensors and solar cell application.

1.3 Problem Statement

Ever since the realization of graphene in the form of carbon nanotube (CNT) can act as an electromechanical actuator in 1999, charge induced actuation of 2D nanomaterials has captured the attention of the scientific community. To understand what an actuator does, our very own muscle, a natural muscle, is the perfect example of actuator with superb performance even though the stress generation ability of natural is as low as 0.35 MPa (Madden, 2004). 2D materials are now being investigated in order to search for a replacement for artificial muscles, also known as electromechanical actuator. 2D materials are potential candidates for electromechanical actuator due to their thermal stability, mechanical flexibility, unique electronic properties and large surface doping (Thanh et al., 2021; van Thanh et al., 2018).

According to Xie *et al.* (2011), 2D graphene was reported to be the primary candidate for electromechanical actuator as it has superior strain that approaches 0.85% . Later, Lu *et al.* (2018) has reported an electromechanical actuator with higher strain of 6.03% and energy density of 11.5 kJ/m^3 using 2D graphydiyne-based 2D materials. For reference, a mammal's skeletal muscle

has energy density of about 8 kJ/m^3 . Unfortunately, none of the materials mentioned above can be employed as artificial muscle in large-scale applications as they are extremely costly to fabricate and laborious to synthesize. As you can see, searching for an alternative 2D actuator material with lesser fabrication cost and larger strain would be a drastic priority in order to artificial muscles to be commercially available.

For this report, first-principle calculations within density functional theory (DFT) are used to calculate the electromechanical properties of 2D TMDC materials as a charge doping function for carrier doping, which are electrons and holes doping. We are selectively interested in the charge induced actuation of NbS_2 and $NbSe_2$ as these materials have been experimentally exfoliated from their bulk form and theoretically proven to exhibit high linear strain and high Young's modulus.

1.4 Aim and Objectives

This FYP aims to study and investigate the electronic and mechanical structure of 2D Niobium based TMDCs which are NbS_2 and $NbSe_2$, plus their electromechanical properties as the result of charge induced actuation materials using first-principle study framework within the scope of density functional theory (DFT). Using first-principles calculations, we investigate electromechanical properties of two-dimensional (2D) hexagonal Niobium based TMDC 2D material. Four objectives have been set to meet this final goal.

The first objective is to carry out literature review on 2D TMDCs as electrode material electromechanical or electrochemical actuator. Literature reviews are required to verify the properties of NbS_2 and $NbSe_2$ on whether they are suitable for large-scale electromechanical or electrochemical actuation applications.

The second objective is to study and carry out literature review on the mechanical and electronic properties of 2D TMDC materials. Literature review is crucial in allowing us to comprehend the properties of 2D NbS_2 and $NbSe_2$,

which will guide us in predicting and understanding the properties of the materials at the end of our research. By simulating the TMDCs layers, the obtained results can be compared with the published results through the literature review and we can verify whether the parameters used are appropriate.

The third objective is to construct the optimized crystal structure of the 2D TMDC materials. This is done obtaining the lattice parameters for NbS_2 and $NbSe_2$ after the literature reviews and having them as PWscf file inputs. The crystal structure parameters can also be obtained from 2dmatpedia via POSCAR format and displaying using XCrySDen.

The fourth objective is to calculate the band structures and density of states (DOS) of the 2D TMDC materials. From the structural parameters, these can be computed using DFT calculations via Quantum Espresso's plane wave function (pw.x). Understanding the stress-strain response of the 2D TMDC materials will provide us the understanding on how much strain can the material withstand before tearing down, and from there, we are able to obtain the maximum strain that we can apply to the 2D TMDC materials to tune its electronic properties, which we can then extend the applicability of the 2D TMDC materials

1.5 Scope and Limitation of the Study

The scope of this study is mainly to investigate the charge induced actuation of 2D TMDC materials NbS_2 and $NbSe_2$. Their crystal structure and electronic properties such as band structures, density of states and lattice parameters are also studied by implementing the Density Functional Theory (DFT). All simulation calculations are carried out under the framework of DFT as implemented in Quantum Espresso using pseudopotentials retrieved from its homepage. The pseudopotentials are of the form of generalized-gradient approximation developed by Perdew-Burke-Ernzerhof (PBE). The cut-off kinetic energy of our plane wave calculations was set to 80 Rydberg throughout the simulation whereas the k points grid used in this simulation were $5 \times 5 \times 1$

for both NbS_2 and $NbSe_2$. Despite having longer computation duration, using higher values of k points grid and cut-off kinetic energy will generate a more accurate result.

I have faced several difficulties and limitations throughout my study for this project. One of the limitations faced is the lack of computational resources and computing power. In order for Quantum Espresso (QE) to compute the DFT calculations, it is recommended to have a 4 core CPU in order for the simulation to run smoothly. Therefore, to compromise with this project, I had to operate on a desktop PC to run all the simulations required as the laptops I have are insufficient in computing power. As a result, I had to sacrifice at least 100 gigabytes of solid-state drive (SSD) storage in order to install and store Ubuntu and Quantum Espresso. SSD storage is not cheap as well, in order to allocate this much space, it is estimated to cost me around RM 150 solely for Ubuntu-Windows dual boot. Furthermore, the denser the k points grid used in the calculation, the longer it will take for the simulation to run. Therefore, as an effort to save time, I have used an adequate $5 \times 5 \times 1$ k points grid for this simulation. However, in order to increase the accuracy of the results, I would have to increase the k points values. This will result in longer wait time and troublesome computing processes.

Another limitation I faced is the lack of experience in using Linux operating system and Ubuntu. The process of installing Ubuntu onto my PC via dual boot was a tedious process and has taken me more than 48 hours to have it successfully installed without any major issues. Installing Ubuntu is very time consuming and there are also various bugs which inhibits my PC from running the operating system smoothly. At the end, I have spent roughly RM1300 to purchase a refurbished HP Z230 workstation for a store recommended by my supervisor solely for Linux and Ubuntu. This way, the issues with Windows-Ubuntu dual boot can be resolved.

CHAPTER 2

THEORETICAL BACKGROUND

2.1 Density Functional Theory (DFT)

When dealing with a many-body problem, it is often said to be tedious and time consuming where the interaction Hamiltonian of all the protons and electrons in the material has to be solved in the electronic ground state. Electronic structure methods can only deal with formidable problem using the fundamental equations for electrons and protons. To ease these troubles, Density Functional Theory (DFT) is then introduced based on the idea of Thomas-Fermi theory of electronic structure of atoms back in 1927. In general, DFT is a framework to approximate and calculate the electronic ground state energy and introduces the concepts of electron density to take into account of the interactions between every particle in the many-body system. DFT is revolutionary as it drastically minimizes the complexity of the computation for the electronic, optical, magnetic and mechanical properties of atomic systems.

2.1.1 Many-Body System

To solve the Density Functional Theory (DFT), a system of numerous interacting electrons and nuclei has to be solved through a many-body Schrödinger equation in order to obtain the electronic properties.

$$H\Psi(\mathbf{r}_1, \mathbf{r}_2, \dots, \mathbf{r}_n, \mathbf{R}_1, \mathbf{R}_2, \dots) = E\Psi(\mathbf{r}_1, \mathbf{r}_2, \dots, \mathbf{r}_n, \mathbf{R}_1, \mathbf{R}_2, \dots) \quad (2.1)$$

The Hamiltonian of a many-body system can be described as:

$$\begin{aligned} \hat{H} = & -\frac{\hbar^2}{2m_e} \sum_i \nabla_i^2 - \sum_{i,l} \frac{e^2 Z_l}{|\mathbf{r}_i - \mathbf{R}_l|} + \frac{1}{2} \sum_{i \neq j} \frac{e^2}{|\mathbf{r}_i - \mathbf{r}_j|} \\ & - \sum_l \frac{\hbar^2}{2M_l} \nabla_l^2 + \frac{1}{2} \sum_{l \neq j} \frac{e^2 Z_l Z_j}{|\mathbf{R}_l - \mathbf{R}_j|} \end{aligned} \quad (2.2)$$

The Hamiltonian can also be denoted into different terms:

$$\hat{H} = \hat{T} + \hat{V}_{ext} + \hat{V}_{int} + E_{II} \quad (2.3)$$

where

$$\hat{T} = -\frac{\hbar^2}{2m_e} \sum_i \nabla_i^2 \quad (2.4)$$

$$\hat{V}_{ext} = -\sum_{iI} \frac{e^2 Z_I}{|\mathbf{r}_i - \mathbf{R}_I|} \quad (2.5)$$

$$\hat{V}_{int} = \frac{1}{2} \sum_{i \neq j} \frac{e^2}{|\mathbf{r}_i - \mathbf{r}_j|} \quad (2.6)$$

$$E_{II} = +\frac{1}{2} \sum_{I \neq J} \frac{e^2 Z_I Z_J}{|\mathbf{R}_I - \mathbf{R}_J|} \quad (2.7)$$

2.1.2 The Hohenberg-Kohn (HK) theorems

DFT's framework is derived from two fundamental theorems by Pierre Hohenberg and Walter Kohn, who are the pioneers of DFT. Known as the Hohenberg-Kohn theorems, the 2 theorems are:

Theorem 1: The external potential, ground state energy and thus the total energy is a unique functional of the electron density. This theorem describes that any ground state electron density can determine the potential and thus all the possible properties of the system, even the many-body system's wavefunction. The universal functional of electron density of Hohenberg-Kohn theorem is defined as:

$$F[n] = T[n] + V_{ee}[n] \quad (2.8)$$

$F[n]$ is the electron density functional where the $T[n]$ represents the kinetic energy functional and $V_{ee}[n]$ represents the Coulombic interaction functional.

Theorem 2: The overall functional that is corresponding to the solutions of the

Schrodinger equation delivers the ground-state energy of the system if and only if the input electron density that minimizes the energy (lowest energy) is the true ground-state electron density. To paraphrase, the energy content of the Hamiltonian will be at the absolute minimum value when the electron charge density is at the ground state. For any electron density that satisfies this integral:

$$\int \rho_t(\mathbf{r})d\mathbf{r} = n \quad (2.9)$$

Then for any positive number of electrons n , the density functional $F[n]$ can be described as

$$E_{v,n}[n] = F[n] + \int v(\mathbf{r})n(\mathbf{r})d^3\mathbf{r} \quad (2.10)$$

2.1.3 The Kohn-Sham equations

We should be able to tell the exact solution for the ground state energy and electron density if we know the exact functional for it. However, it is unfortunate that the HK theorem is still impractical for exact calculations. Therefore, Walter Kohn and Lu Jeu Sham mapped together a system of non-interacting particles from a system of interacting particles with the same electron density.

Now, we can solve the many-body problem via DFT using these steps.

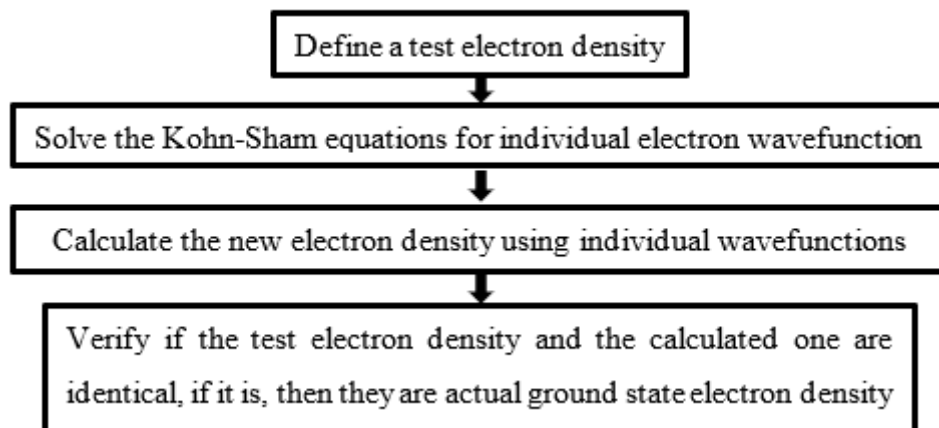


Figure 2.1: General steps to solve the DFT for self-consistency

Figure 2.2 below demonstrates the sequences to solve the self-consistency

solutions using Kohn-Sham equations.

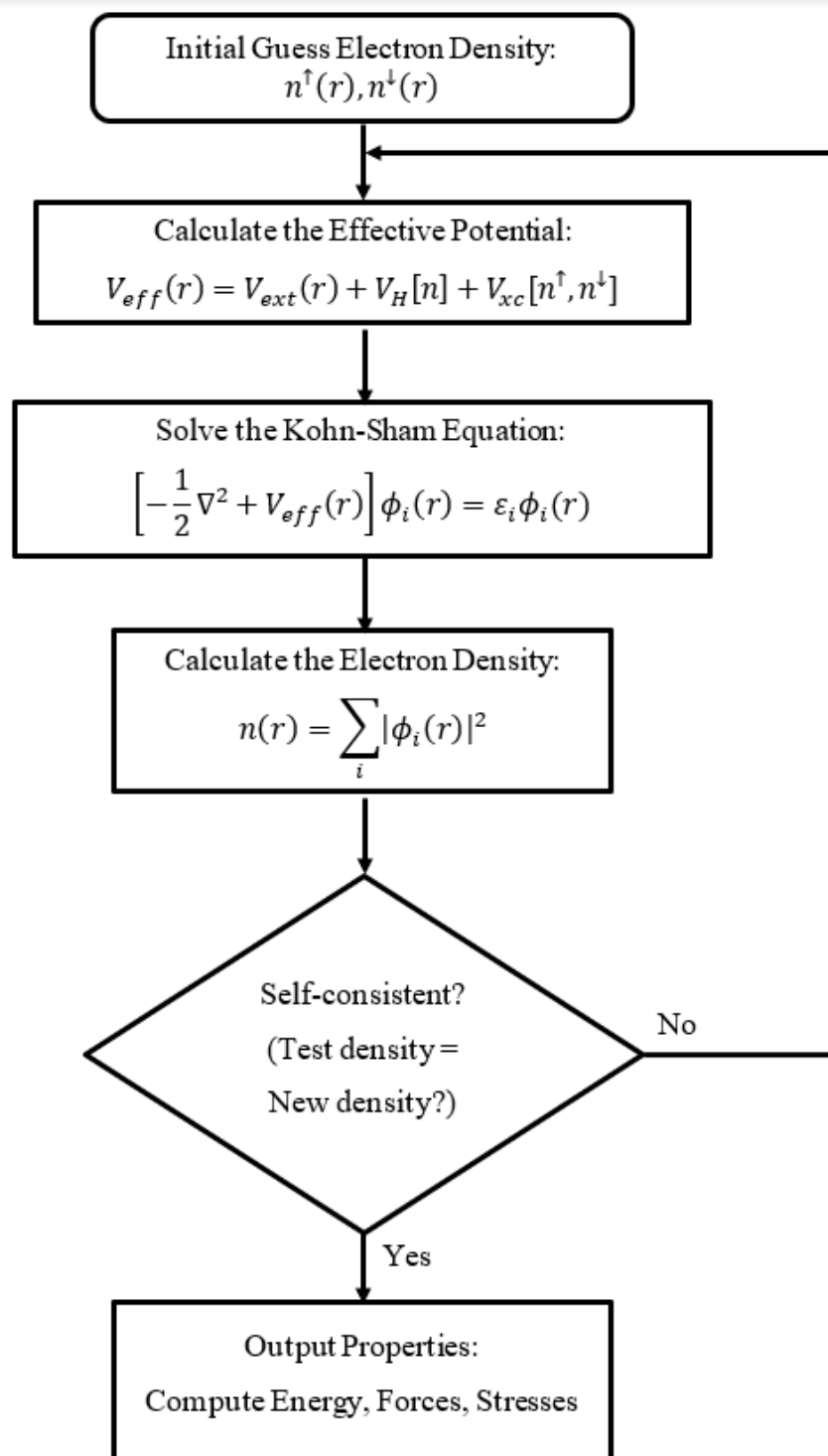


Figure 2.2: Flow chart diagram for obtaining the Self-Consistent Field (SCF) calculation using Kohn-Sham equations

2.1.4 Born-Oppenheimer Approximation

In order to solve the complex many-body time-independent SE above, it is best to consider the wave functions of a diatomic molecule's nucleus and electron to be separated at a fixed distance. Proposed by Max Born and J. Robert Oppenheimer in 1927, the Born-Oppenheimer (BO) approximation assumes that the position of the nuclei in a system is fixed or "static", while solving the SE equation for the dynamic electrons due to the relatively larger mass of nucleus compared to electron. Also known as the adiabatic approximation, the lighter electrons are realized to move much faster than the heavier nuclear ions. Thus, the motion of the two degrees of freedom can be decoupled and the nuclear kinetic energy can be neglected by having nucleus locked in place. Hence, to solve the static nuclear states and energies, the Hamiltonian is reduced to:

$$\hat{H}_{BO} = \sum_{i=1}^N -\frac{\hbar}{2m_i} \nabla_i^2 \psi + \frac{1}{8\pi\epsilon_0} \sum_{i,j;i \neq j}^N \frac{e^2}{|\mathbf{r}_i - \mathbf{r}_j|} - \frac{1}{4\pi\epsilon_0} \sum_{l,i}^N \frac{Z_l e^2}{|\mathbf{l} - \mathbf{r}_i|} \quad (2.11)$$

2.1.5 Band Structure

The band energy of the electrons must be dependent on the wave vector so as the wavefunctions of the electrons, the relation:

$$\epsilon_{n,\mathbf{k}+\mathbf{K}} = \epsilon_{n,\mathbf{k}} \quad (2.12)$$

Which the energy is dependent on the wave \mathbf{k} vectors, also known as the band structure.

2.1.6 Spin-Orbit Coupling

The band structure of crystal lattice is heavily affected by the effect of the spin-orbit (SO) coupling as it lifts the degeneracy for the bands. Due to the coupling of the spin angular momentum of electron in the atom and the orbital angular momentum, the Hamiltonian:

$$\hat{H}_{SO} = -\frac{1}{2m^2c^2} \frac{1}{r} \frac{dV}{dr} \hat{S} \cdot \hat{L} \quad (2.13)$$

In SO coupling treatment in atoms, we treat the system to be a perturbation. The crystal structure's symmetry can heavily influence the SO effects on the crystal structure, it will split the band structure that break the space inversion symmetry.

2.1.7 Density of States (DOS)

The number of energy state per energy per volume, also known as the density of states:

$$g(\epsilon) = \sum_n g_n(\epsilon) \quad (2.14)$$

$$g_n(\epsilon) = \int \frac{d\mathbf{k}}{4\pi^3} \delta(\epsilon - \epsilon_n(\mathbf{k}))$$

2.1.8 Exchange-Correlation (XC) Functional

KS equation is incomplete without the Exchange-Correlation (XC) functional to accurately map the many-body problem onto a system of non-interacting electrons. With the presence of electrons, the Pauli exclusion and motion restriction effect has been taken into account in the system. This calls for the effects exchange and correlation. In Density Functional Theory, we replace the original many-body problem with the effects of exchange and correlation with XC function $E_{XC}(n)$.

DFT approximation was initially approximated using local density approximation (LDA). Regarding on how the DFT scheme is approximated, homogeneous gaseous electron's XC energy is used for this purpose on the XC energy. Only the local electron density is considered, and to be equivalent to the density of the electron gas:

$$E_{XC}^{LDA} = \int d^3\mathbf{r} n(\mathbf{r}) \epsilon_{xc}(n(\mathbf{r})) \quad (2.15)$$

where ε_{xc} is the XC energy density of the homogenous electron gas, where the system is neutral electrically with a uniform positive background charge. The XC energy can then be separated into 2 parts, exchange and correlation:

$$\varepsilon_{xc}(n(\mathbf{r})) = \varepsilon_c(n(\mathbf{r})) + \varepsilon_x(n(\mathbf{r})) \quad (2.16)$$

In the less complicated case of homogenous gaseous electron system, there is only the exchange energy (ε_x) expression but no analytic expression for the correlation energy (ε_c). Occasionally, quantum Monte Carlo (MC) method has to be used to numerically estimate the correlation energy value. The issue with LDA functional is that it consists of errors in energy degeneracy and long-range tails that will lead to local variation. The underestimation of band gaps, large cohesive energy and absorption energy overestimation are drawbacks of LDA which made it impossible to be applied in real system.

Besides LDA, approximation attempts such as Generalized Gradient Approximation (GGA), meta-GGA and Hybrid functional are also implement in DFT to improve upon LDA. Taking the gradient of electron density into account, GGA is sometimes used to approximate the XC energy. GGA is a modification LDA due to the absence of simple functional forms unlike LDA.

$$E_{XC}^{GGA} = \int d^3r n(\mathbf{r}) \varepsilon_{xc}(n(\mathbf{r}), \nabla n(\mathbf{r})) \quad (2.17)$$

Unfortunately, the computational power required for these approximations are much higher than LDA. Not only that, these sophisticated functional doesn't always produce more accurate result compared to LDA. Luckily, different variation of GGA such as s PW91 (Perdew and Wang 1992, Perdew et al. 1992) and advanced version of PW91: PBE (Perdew et al. 1996) are proposed for XC functional. In this case, the Perdew-Burke-Ernzerh (PBE) version of Generalized Gradient Approximation (PBE-GGA) functional is implemented.

2.1.9 Bloch's Theorem

Discovered in 1929 and named after Felix Bloch, the Bloch's theorem defines that in order to solve for the solutions to SE, they have to be in the form of plane

wave modified by periodic functions. These functions are known as Bloch functions, they serve as the electron's basis for the states or wave functions in a crystal.

$$\psi(\mathbf{r}) = e^{i\mathbf{k}\cdot\mathbf{r}} u(\mathbf{r}) \quad (2.18)$$

$\psi(\mathbf{r})$ are the eigenstates of a single-electron Hamiltonian and is specific for a constant reciprocal lattice vector \mathbf{k} . Thus, this wave vector \mathbf{k} can be constrained to the first Brillouin zone of the reciprocal lattice.

2.1.10 Plane Wave

Due to Bloch's theorem, it is obvious for us to use planewaves to solve the KS equations in a many-body system. Using Bloch's theorem, the wavefunction can be expressed in terms of plane waves and the Hamiltonian terms can then be expanded in their Fourier series terms:

$$\sum_{\mathbf{G}'} \left(\frac{1}{2} |\mathbf{k} + \mathbf{G}'|^2 \delta_{\mathbf{G},\mathbf{G}'} + V_{ext}(\mathbf{G} - \mathbf{G}') + V_{Hartree}(\mathbf{G} - \mathbf{G}') + V_{xc}(\mathbf{G} - \mathbf{G}') \right) c_{i,\mathbf{k}+\mathbf{G}'} = \varepsilon_i c_{i,\mathbf{k}+\mathbf{G}} \quad (2.19)$$

The \mathbf{G} represents the reciprocal lattice vectors whereas ε represents the eigenenergy in the KS equation. The $c_{i,\mathbf{k}+\mathbf{G}}$ is the expanded plane waves' coefficient for its wave function. However, if a truncation is not used, the sum of the equation (2.19) can be infinite. Hence, a maximum energy cutoff has to be chosen so the basis set of plane waves can be finite in order for the KS equation to be solved with approximation methods. To solve the plane waves in the system, the number of electrons and cutoff energy heavily influence the computational cost. Therefore, pseudopotentials are implemented in order to lessen the burden of the computational power on the plane wave based DFT calculations.

2.2 Pseudopotential

Pseudopotentials is an approximation method to replace the tight core electrons bonding and strong Coulomb potential with a faint effective potential. The weaker pseudopotential allows the pseudo wavefunctions of the core electrons to be constructed smoothly (Sholl and Stecker, 2009). Pseudopotential is introduced to shorten the computation time to solve the KS equation with many plane waves. Norm-conserving, ultrasoft, and plane-augmented wave (PAW) are the 3 main variations of pseudopotentials.

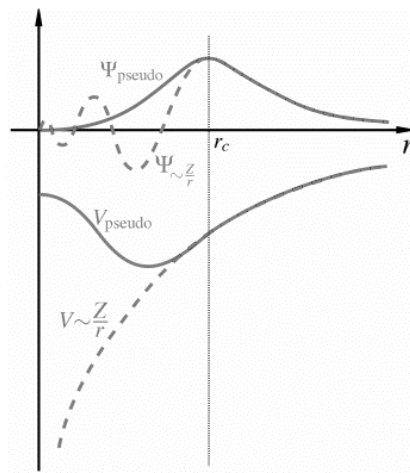


Figure 2.3: A graph of pseudopotential and its corresponding pseudo wavefunction

2.2.1 Norm-conserving pseudopotential

Norm-conserving pseudopotential function is a common but better selection for total energy calculations in modern plane-wave structure codes. Basis-set with lesser cut-off energy can be used:

$$V_{ps}(r) = \sum |Y_{lm}\rangle V_{lm}(r) \langle Y_{lm}| \quad (2.20)$$

The superiority of this method can smooth out the wave function by enforcing 2 conditions: norm of each pseudo-wavefunction are identical inside cut-off radius and all electron and pseudo wavefunctions are identical outside.

CHAPTER 3

LITERATURE REVIEW

3.1 Niobium Disulphide (NbS₂)

Out of the plethora of 2D TMDCs material family, the first material that we are interested in is niobium disulphide. IUPAC name, Niobium (IV) disulphide (NbS₂), has attracted international attention for its enticing properties, anisotropic structure, and versatile application prospects. NbS₂ appears as a black-greyish coloured solid crystal layer that undergoes the same mechanical exfoliation process to obtain its ultrathin 2D form like any other TMDCs. With a molar mass of 157.038 g/mol, density of 4.4 g/cm³ and magnetic susceptibility (χ) of $+120 \cdot 10^{-6} \text{ cm}^3/\text{mol}$ (Lide, D.R. ed., 2005), NbS₂ layer exhibits a wide variety of electronic properties such as superconductivity, semiconducting characteristics and modifiable compositions where its physical and electronic properties can be influenced. The crystal structure of NbS₂ is shown in Fig. 3.1 below.

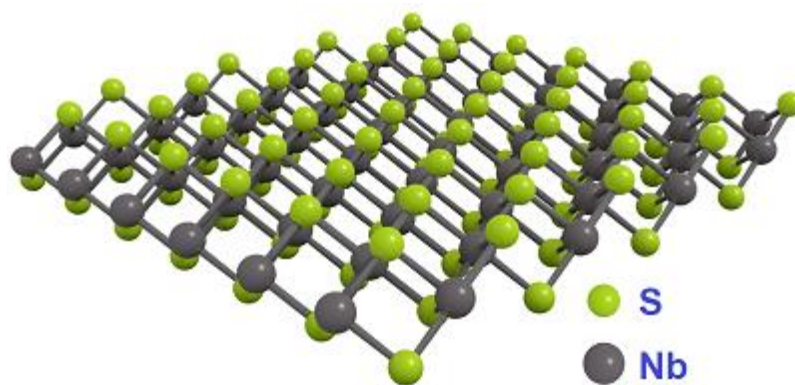


Figure 3.1 Crystal structure of NbS₂ (Ossila)

3.1.1 Structural Properties

NbS₂ comprises of quasi-two-dimensional layered structure, in other words, niobium (Nb) and sulphur form the sheets of NbS₂ in the (*ab*)-plane in the form of S-Nb-S and stack on one another along *c*-plane. Fig. 3.1 above shows the atomic structure of 1T (trigonal) phase of NbS₂. Depending on the film thickness

from exfoliation process, NbS₂ could exist in 3 different general phase or stacking polytypes: 1T (trigonal), 2H(hexagonal), and 3R (rhombohedral). The hexagonal 2H- NbS₂ phase is the most common polytype where the hexagonal layers of S atoms stack one over another known as hexagonal packing with the sites between S atoms layers occupied by Nb in a trigonal-prismatic formation, thus forming a sandwiched layer structure. The interlayers are bound by van der Waals forces, which are weak forces, hence bulk NbS₂ can be mechanically or liquid chemically exfoliated to obtain its 2D TMDCs nanosheets. Fig. 3.2 below shows the atomic crystal structure of each different types of phases for TMDCs.

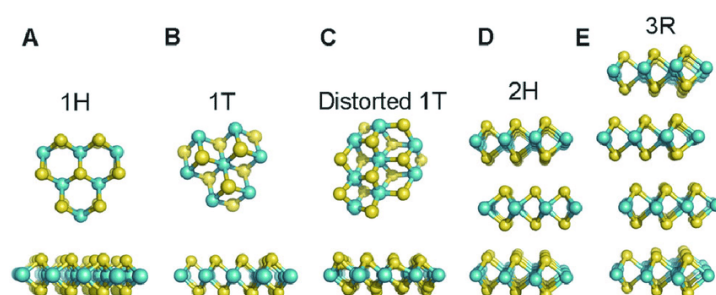


Figure 3.2: Types of TMDCs crystal structure and phases where transition metal atoms are shown in blue and chalcogen atoms are shown in yellow (Kim & Lee, 2018)

According to Ossila, a chemical and material science supplier company, the two most commonly used and major types of packing are 2H- NbS₂ and 3R- NbS₂ as 1T phase is thermodynamically unfavoured. The crystal structure of 2H- and 3R- phase NbS₂ from various sources are shown in Table 3.1 below. Based on literature review, we can observe that the published values of the lattice parameters for both 2H-phase and 3R-phase have acceptable agreement.

Sulphide	Phase	Space group	$a = b$ (Å)	c (Å)	Sources
NbS ₂	2H- NbS ₂	P6 ₃ /mmc	3.310	11.89	Jellinek <i>et al</i>
Nb _{1,39} S ₂	2H- NbS ₂	P6 ₃ /mmc	3.308	12.71	Kadijk & Jellinek
NbS ₂	3R- NbS ₂	R3m	3.330	17.91	Morosin
Nb _{1,06} S ₂	3R- NbS ₂	R3m	3.329	17.91	Powell & Jacobson

Table 3.1: Some examples of different types of phases and packings in NbS₂

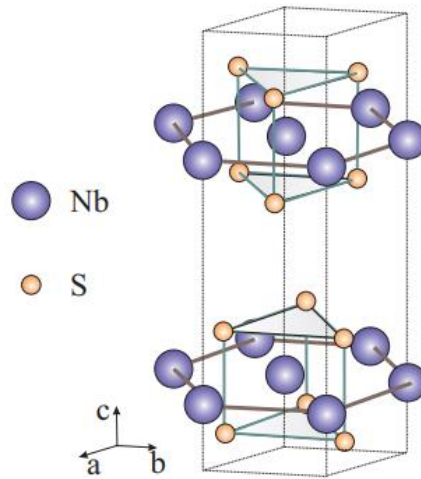


Figure 3.3: Crystal structures of 2H- NbS₂ (Tissen *et al.*, 2013)

According to Tissen *et al.* (2013), the lattice parameters can be agreed upon comparison as $a = 3.321 \text{ \AA}$ and $c = 11.761 \text{ \AA}$. Fig 3.3 shown a 2H- NbS₂ packing in general that has hexagonal symmetry and contains 2 layers of trigonal prisms flipped 180° with respect to each other.

3.1.2 Electronic Properties

The band structure and density of states of 2H- NbS₂ are shown below.

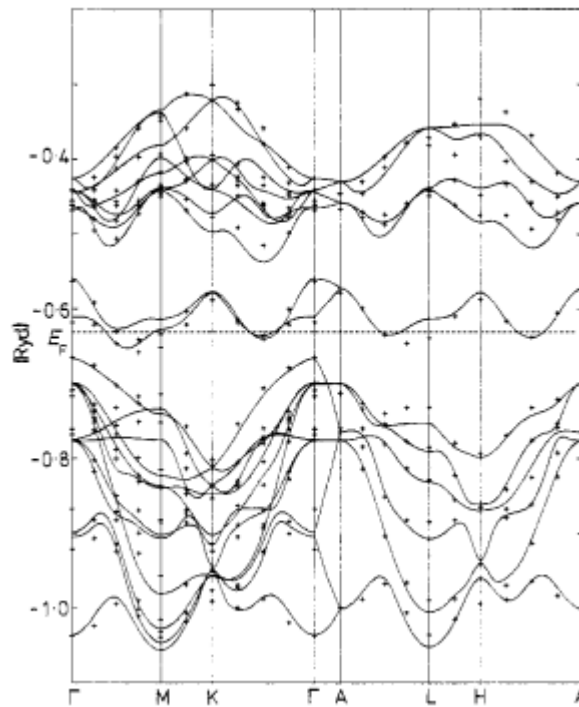


Figure 3.4: Electronic Band Structure of 2H- NbS₂ (Doran *et al.*, 2001)

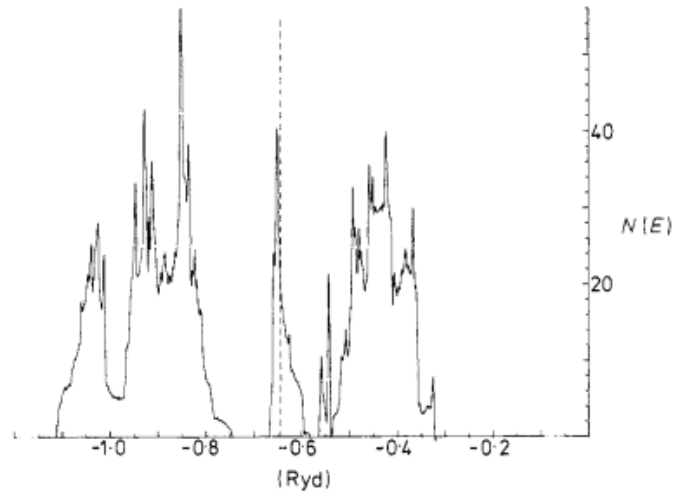


Figure 3.5: Density of States (DOS) of 2H- NbS₂ (Doran *et al.*, 2001)

According to Ossila, 2H- NbS₂ and 3R- NbS₂ exhibit metallic properties. More interestingly, 2H- NbS₂ polytype is a superconducting material with critical temperature of 6 K. As we can see from Fig. 3.4 above, the fermi energy level is not lying at the peak DOS according to Mattheiss but rather on the high-energy side of an asymmetric curve. The saddle point at gamma causes a shoulder beyond the fermi energy level.

As for the charge-induced electronic properties, Yanmei Zang *et.al.* have performed the first principles calculations on NbS₂ under the strain effect from -5% to 5% shown in Fig. 3.6 below.

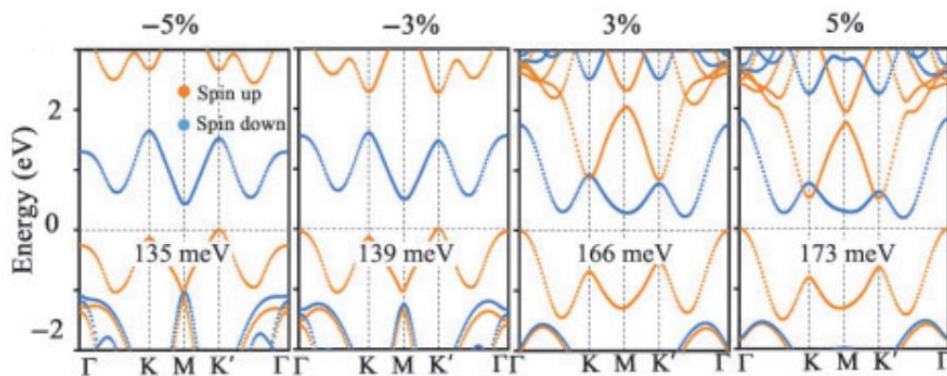


Figure 3.6: Band structures of NbS₂ under external strain ranging from -5% to 5% (Yanmei Zang, Yandong Ma, 2020)

Zang, Yanmei & Ma, Yandong & Peng, Rui & Wang, Hao & Huang, Baibiao & Dai, Ying. (2020). Large valley-polarized state in single-layer NbX₂ (X = S, Se): Theoretical prediction. *Nano Research*. 14. 10.1007/s12274-020-3121-1.

3.1.3 Mechanical Properties

Hao Sun et. al. have calculated all the linear mechanical properties for NbS₂. Table 3.2 below shows their mechanical properties and elastic properties. The literature review compares the DFT calculated mechanical properties, including elastic constants ($C_{11}, C_{22}, C_{12}, C_{21}$), 2D strain (ε), 2D layer modulus (γ), Young's modulus (Y), and Poisson's ratio (ν). All moduli are in unit of N/m.

[N/m]	C_{11}	C_{22}	C_{12}	C_{21}	ε_x	ε_y	γ	Y_{10}	Y_{01}	ν_{10}	ν_{01}
NbS ₂	90.09	90.03	25.61	22.12	0.23	0.23	57.85	82.81	82.81	0.28	0.28
(Mater. Adv., 2021, 2, 6631)											
NbS ₂	112.79	109.20	38.58	33.91	-	-	-	99.15	96.00	-	-
(ACS Omega 2021, 6, 2956–2965)											

Table 3.2: DFT calculated mechanical properties for NbS₂ (Hao Sun et.al., 2021)

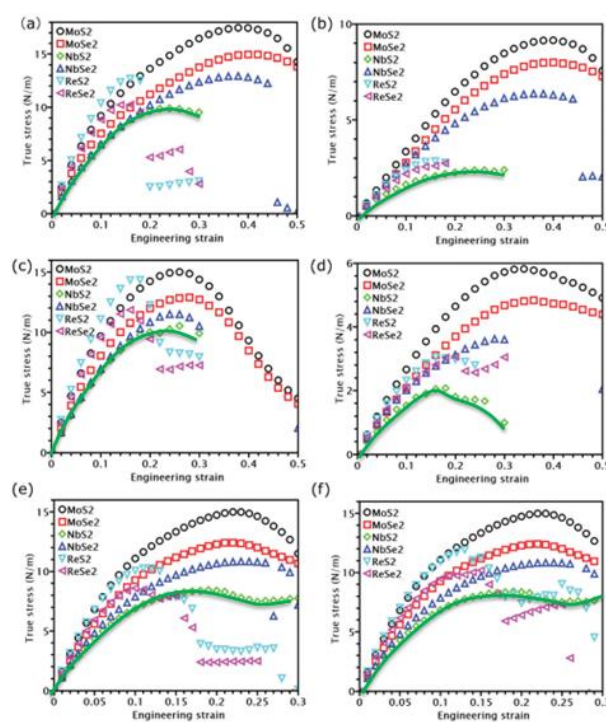


Figure 3.7: Stress-strain curves of NbS₂ highlighted in green (a) and (b) x-uniaxial tension, (c) and (d) y-uniaxial, (e) and (f) biaxial along x and y directions respectively. (Hao Sun et.al., 2021)

3.2 Niobium Diselenide (NbSe₂)

Similar to NbS₂, the next material that we are interested in is niobium diselenide. IUPAC name, Niobium (IV) diselenide (NbSe₂), has attracted international attention for its enticing properties, anisotropic structure, and versatile application prospects. NbSe₂ appears as a gray coloured solid crystal layer that undergoes the same mechanical exfoliation process to obtain its ultrathin 2D form like any other TMDCs. With a molar mass of 250.83 g/mol, density of 6.3 g/cm³ and melting point of over 1300°C (Haynes & William, 2011). NbS₂ layer exhibits a wide variety of electronic properties such as superconductivity, semiconducting characteristics and modifiable compositions where its physical and electronic properties can be influenced. The crystal structure of NbS₂ is shown in Fig. 3.8 below.

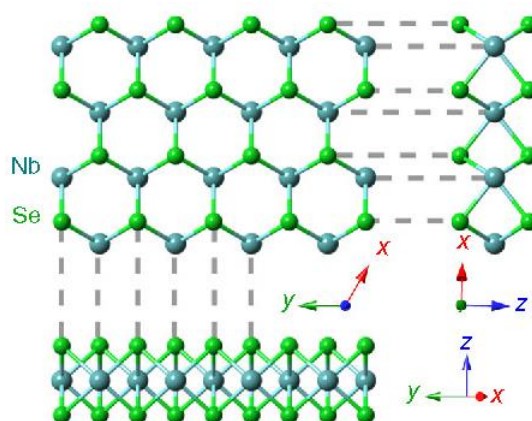


Figure 3.8 Crystal structure of NbSe₂ (Hong Wang *et al.*, 2017)

3.2.1 Structural Properties

NbSe₂ comprises of quasi-two-dimensional layered structure, in other words, niobium (Nb) and Selenium (Se) form the sheets of NbSe₂ in the (*ab*)-plane in the form of Se-Nb-Se and stack on one another along *c*-plane. Fig. 3.8 above shows the atomic structure of 2H (hexagonal) phase of NbSe₂. Depending on

the film thickness from exfoliation process, NbSe₂ could exist in 3 different general phase or stacking polytypes: 1T (trigonal), 2H(hexagonal), and 3R (rhombohedral). The hexagonal 2H- NbSe₂ phase is the most common polytype where the hexagonal layers of Se atoms stack one over another known as hexagonal packing with the sites between Se atoms layers occupied by Nb in a trigonal-prismatic formation, thus forming a sandwiched layer structure. The interlayers are bound by van der Waals forces, which are weak forces, hence bulk NbSe₂ can be mechanically or liquid chemically exfoliated to obtain its 2D TMDCs nanosheets.

As shown in Fig. 3.9 below, the crystal structure of 2H-NbSe₂ of space group P6₃/mmc can be seen. According to Sidoumou *et al.* (2021), the unit cell dimensions for this structure are $a = 3.4475 \text{ \AA}$ and $c = 12.5702 \text{ \AA}$. According to Fisher & Sienko (1980), they are non-stoichiometric. For 2H-NbSe₂, the Nb atoms are sandwiched directly upon one another along the c axis, which is not the case for 3R-NbSe₂.

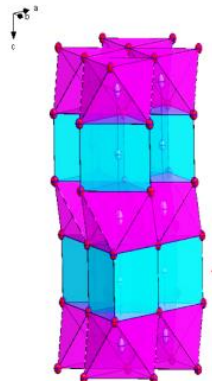


Figure 3.9: Crystal structure of 2H- NbSe₂ (Sidoumou *et al.*, 2021),

Polytype	Space group	$a = b$ (Å)	c (Å)
2H-NbSe ₂	P6 ₃ /mmc	3.463	13.210
2H-Nb _{1,1} Se ₂	P6 ₃ /mmc	3.470	13.807
3R-NbSe ₂	R3m	3.506	19,708
3R-Nb _{1,1} Se ₂	R3m	3.412	21.679

Table 3.3: Some examples of different types of phases and packings in NbSe₂
(Sidoumou *et al.*, 2021)

3.2.2 Electronic Properties

The band structure and density of states of 2H- NbSe₂ are shown below.

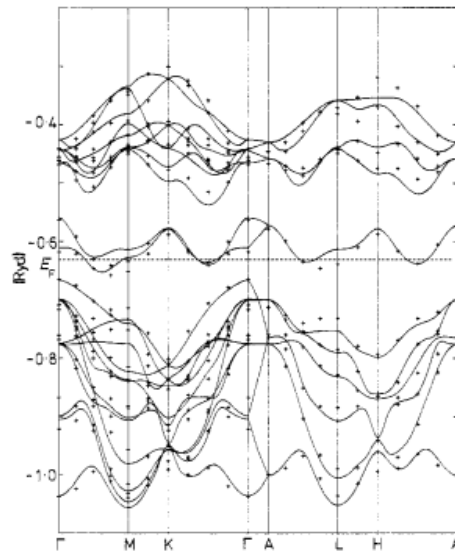


Figure 3.10: Electronic Band Structure of 2H- NbSe₂ (Doran *et al.*, 2001)

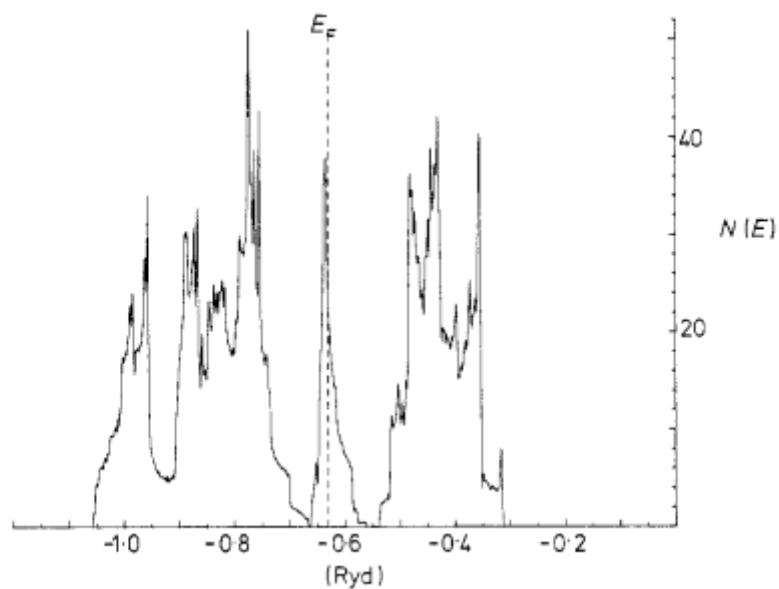


Figure 3.11: Density of States (DOS) of 2H- NbSe₂ (Doran *et al.*, 2001)

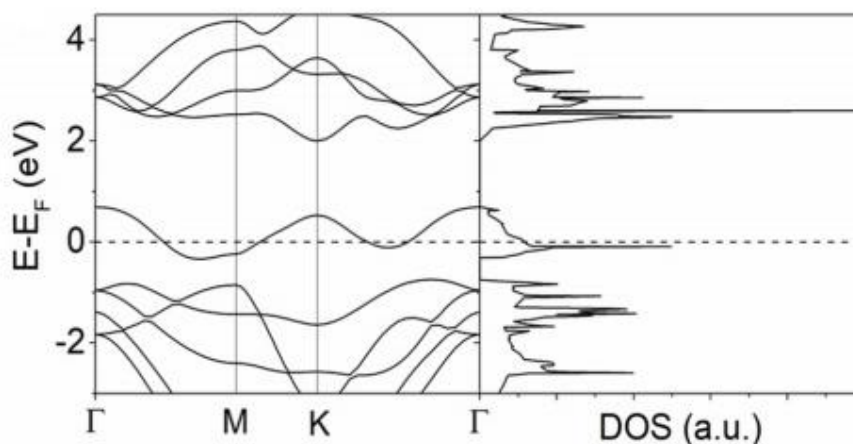


Figure 3.12: Electronic band structures and DOS of the relaxed 2D NbSe₂ (Yeoh *et al.*, 2020)

As for the charge-induced electronic properties, Yanmei Zang *et al.* have performed the first principles calculations on NbSe₂ under the strain effect from -5% to 5% shown in Fig. 3.13 below.

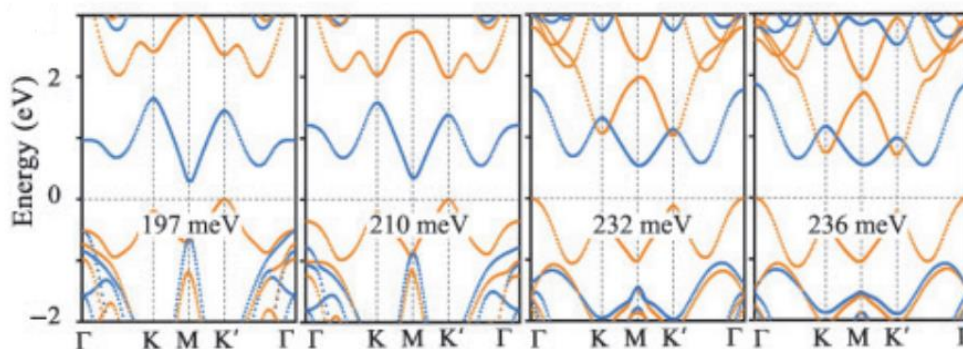


Figure 3.13: Band structures of NbSe₂ under external strain ranging from -5% to 5% (Yanmei Zang, Yandong Ma, 2020)

3.2.3 Mechanical Properties

Hao Sun *et al.* have calculated all the linear mechanical properties for NbSe₂. Table 3.4 below shows their mechanical properties and elastic properties. The literature review compares the DFT calculated mechanical properties, including elastic constants ($C_{11}, C_{22}, C_{12}, C_{21}$), 2D strain (ϵ), 2D layer modulus (γ), Young's modulus (Y), and Poisson's ratio (ν). All moduli are in unit of N/m.

[N/m]	C_{11}	C_{22}	C_{12}	C_{21}	ϵ_x	ϵ_y	γ	Y_{10}	Y_{01}	ν_{10}	ν_{01}
NbSe₂	86.58	89.53	30.74	28.47	0.37	0.25	57.85	75.67	75.67	0.36	0.36
NbSe₂	83.27	87.96	30.64	32.42	-	-	-	72.61	76.68	-	-

Table 3.4: DFT calculated mechanical properties for NbSe₂ (Hao Sun et.al., 2021)

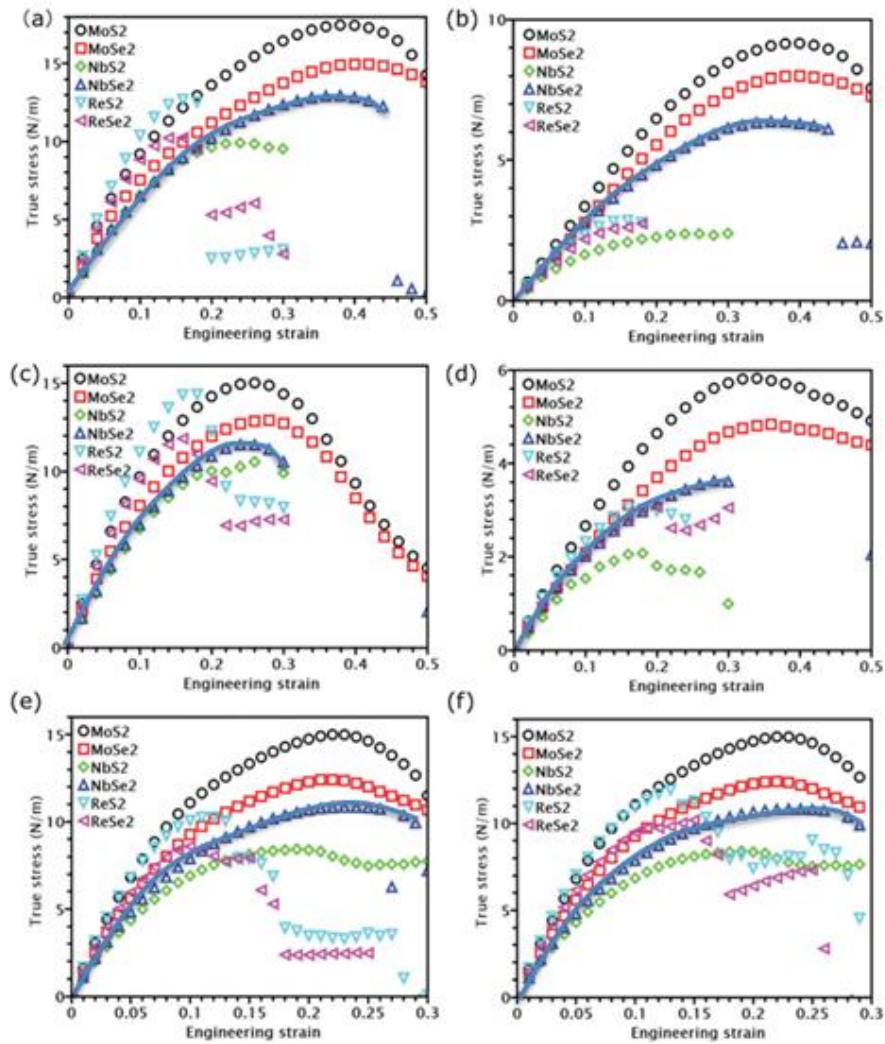


Figure 3.14: Stress-strain curves of NbSe₂ highlighted in blue (a) and (b) x-uniaxial tension, (c) and (d) y-uniaxial, (e) and (f) biaxial along x and y directions respectively.

CHAPTER 4

METHODOLOGY AND WORK PLAN

4.1 DFT calculation with Quantum ESPRESSO

Throughout this research project, an open-source package codes for electronic-structure research calculations and modelling, Quantum Espresso (QE), is implemented for DFT calculations. Quantum Espresso is actually an acronym for Quantum Open-Source Package for Research Electronic Structure, Simulation and Optimization (Giannozzi, 2009). Fig. 4.1 below shows the logo of QE. In order to run this package, it is mandatory to have a Linux-based operating system like Ubuntu, although there is some software out there that are capable of running QE on Windows. On the other hand, to determine the electronic structure and crystal materials at quantum level, VASP is a better DFT calculating package than QE. However, QE is chosen over VASP here due to the fact that it's free to use and more accessible for undergraduate students.



Figure 4.1: Quantum ESPRESSO. (Giannozzi, 2009)

4.2 Visualization of crystal structure with XCrySDen

What Quantum Espresso does only is applying the plane wave (PW) density functional theory (DFT) along with pseudopotentials and periodic boundary conditions. In order to visualize the atomic structure and geometries generated from QE, we need to use one more software package known as XCrySDen (Kokalj, 1999). XCrySDen is utilized to display the atomic structure modelled from PWscf input or output files. Furthermore, we can also measure the distance between atoms and also vary the bond angles. After the crystal structure is geometrically relaxed via QE's VC-relax, XCrySDen is helpful in aiding us

verifying and determining the atomic geometry and positions. Fig. 4.2 shows the user interface of XCrySDen and Fig. 4.3 demonstrates on how the bond distance is observed and measured.

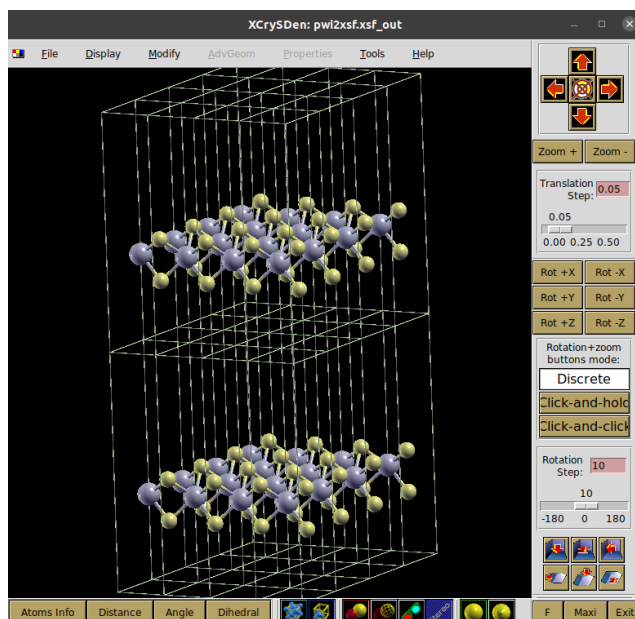


Figure 4.2: XCrySDen's User Interface

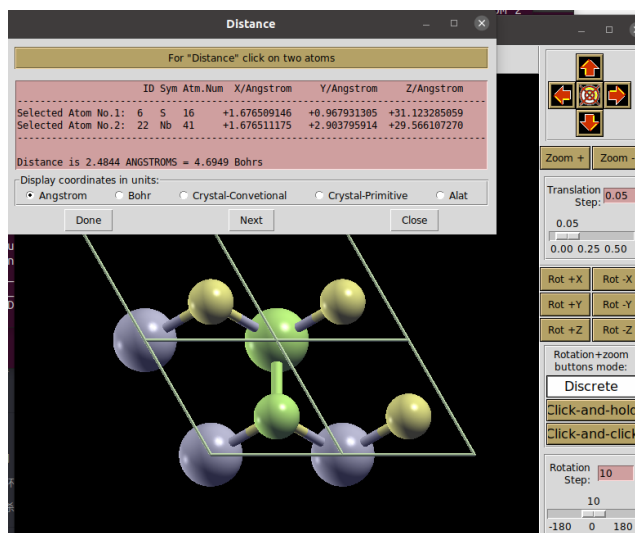


Figure 4.3: Interface of Measuring the Atomic Distance using XCrySDen.

4.3 Performing Calculations

QE can perform various types of calculations, from self-consistent field (SCF) calculation to density of states. QE is also capable of calculating the electronic structure and total energy in Rydberg by implementing the plane-wave basis sets and pseudopotential techniques. Density Function Theory (DFT) calculations with Perdew-Burke-Ernzerhof (PBE) (Perdew, Burke, Ernzerhof, 1996) generalized gradient approximation (GGA) functional are performed in QE. Fig. 4.4 shows the input file that consists of the necessary parameters which is required for any QE calculation. For SCF calculation, the convergence threshold for total force, total energy has to be specified. Other than that, the crystal structure properties have to be defined, this includes lattice vector, cell parameters, atomic positions, atomic species, atomic weight, pseudopotential and k-point grid. In general, after the necessary input file is written, run the codes by using the command in a Linux terminal as shown in Fig. 4.5.

(a)

```

1 &CONTROL
2     calculation = 'scf',
3     restart_mode = 'from_scratch',
4     outdir = './scf',
5     pseudo_dir = './',
6     prefix = 'NbSe',
7     tstress = .true.,
8     tprnfor = .true.,
9     etot_conv_thr= 1.00-4,
10    forc_conv_thr= 1.00-3,
11    nsteps=500,
12 /
13 &SYSTEM
14     tbrav = 0,
15     cellldm(1) = 6.35250587,
16     nat = 3,
17     ntyp = 2,
18     ecutwfc = 80,
19     occupations = 'smearing',
20     smearing = 'mv',
21     degauss = 0.01,
22 /
23 /
24 &ELECTRONS
25     conv_thr = 1.0d-7,
26     mixing_beta = 0.3,
27 /
28 &IONS
29     ion_dynamics = 'bfgs',
30 /
31 /
32 &CELL
33     cell_dynamics = 'bfgs',
34     cell_dofree = '2Dxy',
35 /
36 /
37 ATOMIC_SPECIES
38 Nb  92.90638  Nb_ONCV_PBE_sr.upf
39 Se  78.96   Se_ONCV_PBE_sr.upf
40 CELL_PARAMETERS (alat)
41  1.036406459  0.000624771  0.000000000
42  0.517602183  0.097666318  0.000000000
43  0.000000000  0.000000000  5.155445000
44 /
45 ATOMIC_POSITIONS (angstrom)
46 Nb  1.852373829          11.6850866471
47 Se  3.5954600065       2.0758400068    10.0163323739
48 Se  3.5954330160       2.0758248395    13.3536495789
49 K_POINTS automatic
50 5 5 1 0 0 0
51

```

(b)

```

1 &CONTROL
2     calculation = 'vc-relax',
3     restart_mode = 'from_scratch',
4     outdir = './vcrelax',
5     pseudo_dir = './',
6     prefix = 'NbSe',
7     tstress = .true.,
8     tprnfor = .true.,
9     etot_conv_thr= 1.00-4,
10    forc_conv_thr= 1.00-3,
11    nsteps=500,
12 /
13 &SYSTEM
14     tbrav = 0,
15     cellldm(1) = 6.35250587232627,
16     nat = 3,
17     ntyp = 2,
18     ecutwfc = 80,
19     occupations = 'smearing',
20     smearing = 'mv',
21     degauss = 0.01,
22 /
23 /
24 &ELECTRONS
25     conv_thr = 1.0d-7,
26     mixing_beta = 0.3,
27 /
28 &IONS
29     ion_dynamics = 'bfgs',
30 /
31 /
32 &CELL
33     cell_dynamics = 'bfgs',
34     cell_dofree = '2Dxy',
35 /
36 /
37 ATOMIC_SPECIES
38 Nb  92.90638  Nb_ONCV_PBE_sr.upf
39 Se  78.96   Se_ONCV_PBE_sr.upf
40 CELL_PARAMETERS (alat)
41  1.000000  0.000000  0.000000
42  0.500000  0.866025  0.000000
43  0.000000  0.000000  5.155445
44 ATOMIC_POSITIONS (angstrom)
45 Nb  1.745725254  1.007894992  11.685603620
46 Se  3.491455746  2.015793008  9.999692397
47 Se  3.491455746  2.015793008  13.369691983
48 K_POINTS automatic
49 5 5 1 0 0 0

```

Figure 4.4: Input file for (a) SCF calculation and (b) Geometrical Relaxation via QE

```

eltonmah@eltonmah-HP-Z230-SFF-Workstation: ~/NewVcrelax
eltonmah@eltonmah-HP-Z230-SFF-Workstation:~/NewVcrelax$ mpirun -np 4 /home/eltonmah/Downloads/qe-6.8/bin/pw.x <NbS.scf.in> NbS.scf.out

```

Figure 4.5: Command to initiate the computation via Linux Terminal

4.4 High Symmetry Point

In order to calculate the band structure and density of states, high symmetry k point has to be determined and stated in the input file. Figure 4.6 below shows the Brillouin Zone (BZ) and the high symmetry points for a hexagonal lattice.

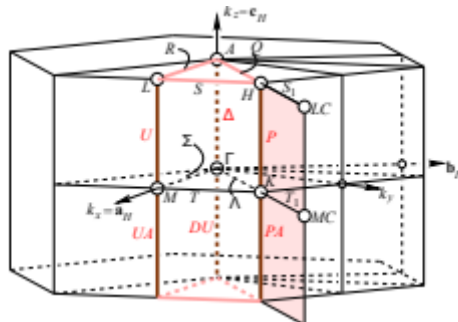


Figure 4.6: Brillouin Zone for a Hexagonal System (Retrieved from Bilbao crystallographic server)

Using XCrySDen, the high symmetry points that I have chosen to use are: Γ , K, M with path $\Gamma \rightarrow K \rightarrow M \rightarrow \Gamma$ as shown in Fig. 4.6 below.

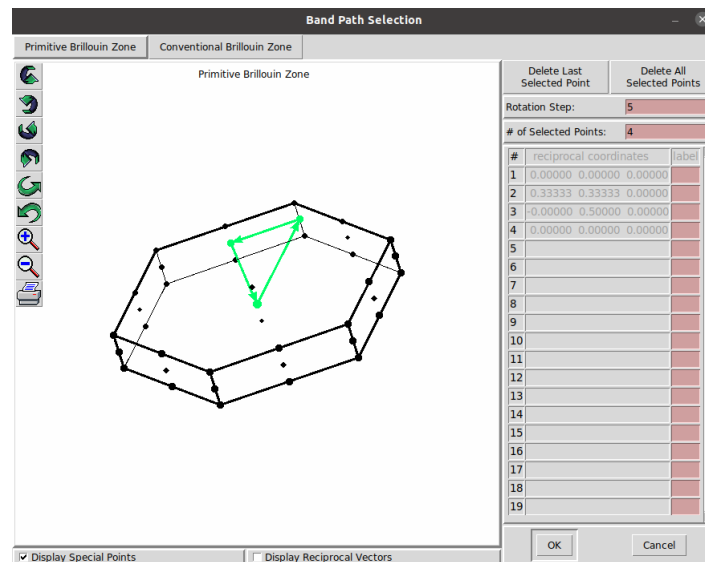


Figure 4.7: XCrySDen k-path selection

```
K_POINTS {crystal_b}
4
0.0000 0.0000 0.000 20 !G
0.3333 0.3333 0.000 20 !K
0.0000 0.5000 0.000 20 !M
0.0000 0.0000 0.000 20 !G
```

Figure 4.8: High Symmetry k-points

4.5 Work Plan

Three main steps are used to perform the calculation and data collections. The first step is the calculation for electronic properties and structural optimization of crystal structure. The second step involves the investigation of actuator performance with stress-strain calculations. Last but not least, the third step is to study the mechanical properties of these materials.

4.5.1 Structural Optimization and Electronic Properties Calculation

We first perform DFT calculations using Quantum Espresso with the flowchart shown in Figure 4.9 below.

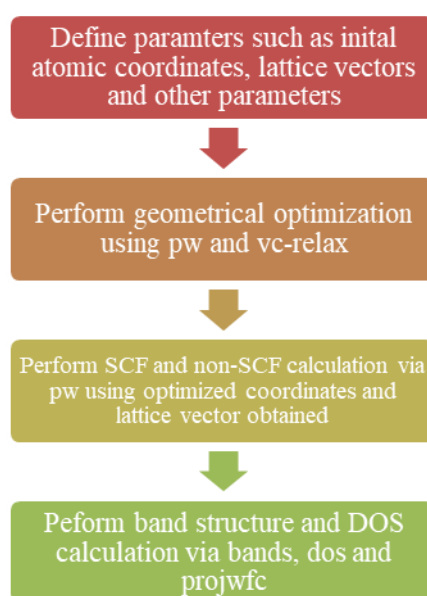


Figure 4.9: Flowchart of DFT calculation using Quantum Espresso for electronic and structural properties

We then plot the band structure and density of state (DOS) graph after this step by transferring the data collected from bands and dos to mathematical plotting softwares.

4.5.2 Calculation of Actuator Performance

In this step, the variable-cell relation calculation is performed for both NbS₂ and

NbSe₂ under charge doping. Using 0.03 e/atom increment, the range of total charge doping per atom is from +0.12 e/atom to -0.12 e/atom. Figure 4.10 below shows a variable line of total charge named “tot_charge” to indicate the injection of a number of charges into the system. With the addition of the total charge injected in the input file, a total of 9 set of data are expected from each material.

```

/
&SYSTEM
      ibrav = 0,
      celldm(1) = 6.35942227269893,
      nat = 3,
      ntyp = 2,
      ecutwfc = 80,
      nosym=.true.
      occupations = 'smearing' ,
      smearing = 'mv' ,
      degauss = 0.01 ,
      tot_charge = 0.12

```

Figure 4.10: Inserting a total charge of 0.12 into the input file

On the other hand, the strain ε induced by the charge injection is calculated using the equation below:

$$\varepsilon = \frac{a_{charged} - a_0}{a_0} \quad (4.1)$$

where a is the lattice parameter of the charge-doped material whereas a_0 refers to the neutral lattice parameter. If the strain is a negative value, it indicates a compressive strain whereas if the strain is a positive value, it indicates a tensile strain. The strain against charge per atom graphs are then plotted.

4.5.3 Calculation of Mechanical Properties

-0.6% to +0.6% of strain in the biaxial direction, along the xx direction and along the yy direction is applied with interval of 0.2% to determine three sets of strain data with each set consisting of seven subsets of cell parameters. Then, relaxation calculation is performed on the materials and the energy of the material is obtained at various strain values. A polynomial curve fit of degree of 2 is then plotted. The Young's Modulus and Poisson's ratio of the NbS₂ and

NbSe₂ is obtained using these calculations. 3 sets of parabolic curves, biaxial strain, strain along xx direction and strain along yy direction graphs are curve fitted using:

$$\text{For xx direction, } W_{xx} = c_{xx} + a_{xx}z^2 + b_{xx}z \quad (4.2)$$

$$\text{For yy direction, } W_{yy} = c_{yy} + a_{yy}z^2 + b_{yy}z \quad (4.3)$$

$$\text{For biaxial, } W_{bi} = c_{bi} + a_{bi}z^2 + b_{bi}z \quad (4.4)$$

The parabolic curves are plotted to obtain the a, b and c value. Note that the value for b should be very small.

The energy equation in the material is expressed as:

$$E = E_0 + \frac{1}{2}C_{11}\varepsilon_{xx}^2 + \frac{1}{2}C_{22}\varepsilon_{yy}^2 + C_{12}\varepsilon_{xx}\varepsilon_{yy} \quad (4.5)$$

The E_0 denotes the energy of the material at neutral condition while C_{11} is the linear elastic constant along xx direction, C_{22} is the linear elastic constant along yy direction and ε refers to the strain. When in the case of xx direction strain:

$$\varepsilon_{yy} = 0$$

Fitting into equation (4.2), then

$$c_{11} = 2a_{xx}$$

Based on Quantum ESPRESSO's standard unit of operation, the total energy has to be in the unit of Rydberg, thus the elastic constant value has to be converted to SI unit:

$$C_{11} = c_{11} \times \frac{13.61 \times 1.6 \times 10^{-19}}{A} \quad (4.6)$$

Where A refers to the area of the unit cell in m^2 calculated via cross product of the cell parameter vectors.

On the other hand, when in the case of yy direction strain:

$$\varepsilon_{xx} = 0;$$

Fitting into equation (4.3), then: $c_{22} = 2a_{yy}$

Based on Quantum ESPRESSO's standard unit of operation, the total energy has to be in the unit of Rydberg, thus the elastic constant value has to be converted to SI unit:

$$C_{22} = c_{22} \times \frac{13.61 \times 1.6 \times 10^{-19}}{A}$$

Last but not least, when in the case of biaxial strain:

$$\varepsilon_{xx} = \varepsilon_{yy}$$

Fitting into equation (4.4), then

$$c_{12} = a_{bi} - \frac{1}{2}c_{11} - \frac{1}{2}c_{22}$$

$$c_{12} = a_{bi} - a_{xx} - a_{yy}$$

Based on Quantum ESPRESSO's standard unit of operation, the total energy has to be in the unit of Rydberg, thus the elastic constant value has to be converted to SI unit:

$$C_{12} = (a_{bi} - a_{xx} - a_{yy}) \times \frac{13.61 \times 1.6 \times 10^{-19}}{A}$$

After obtaining C_{11} , C_{22} , C_{12} , Young's modulus (Y_{01} & Y_{10}) and Poisson's ratio can then be calculated using:

$$Y_{10} = \frac{C_{11}C_{22} - C_{12}^2}{C_{22}}$$

$$Y_{01} = \frac{C_{11}C_{22} - C_{12}^2}{C_{11}}$$
(4.7)

$$v_{10} = \frac{C_{12}}{C_{22}}$$

$$v_{01} = \frac{C_{12}}{C_{11}}$$
(4.8)

where v_{10} and v_{01} are the Poisson's ratio in the xx and yy directions respectively. The values required for the stress-strain curve can be obtained from the diagonal element of the Cauchy stress tensor of both NbS₂ and NbSe₂.

CHAPTER 5

RESULTS AND DISCUSSIONS

5.1 Niobium Disulphide (NbS_2)

First and foremost, the three-dimensional crystal structure is constructed by having its cell parameters and atomic position input into the NbS.scf.in file. The material parameter is obtained from the website 2dmatpedia where 2dm-3019 is the material ID for this NbS_2 . This NbS_2 is a hexagonal 2H-phase polytype and belonging to the space group P-6m2. The pseudopotential files used to perform the calculations are Nb_OCNV_PBE_sr.upf and S_OCNV_PBE_sr.upf. These pseudopotential codes are optimized norm-conserving Vanderbilt pseudopotential (ONCV or OCNV) scalar-relativistic version produced by D.R. Hamann. The crystal structure is then visualized using XCrySDen as shown in Fig. 5.1 below.

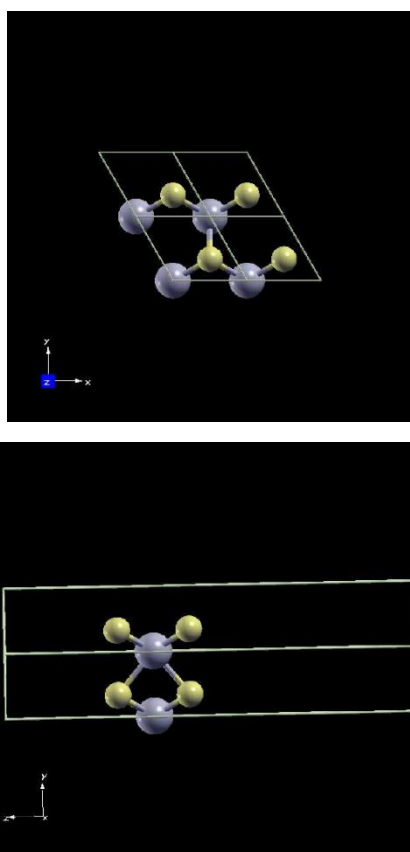


Figure 5.1: Top and Side view of NbS_2 atomic structure from XCrySDen

5.1.1 Convergence Tests

The optimum cut-off kinetic energy and k-point mesh have to be determined before any band structure calculations can be performed. As shown in Fig. 5.2 below, the convergence calculations for cut-off kinetic energy (E_{cutwfc}) are done by performing multiple series of calculations for the total energy while varying the cut-off kinetic energy input and fixed the k-points mesh at $5 \times 5 \times 1$. The total energy is then plotted in relation to the cut-off kinetic energy, thus showing a curve that converges towards a constant value. As you can see, the total energy converges after 40 Ry point and remain relatively constant through 60Ry to 100 Ry. From SCF calculation, its fermi energy is -0.9077 eV.

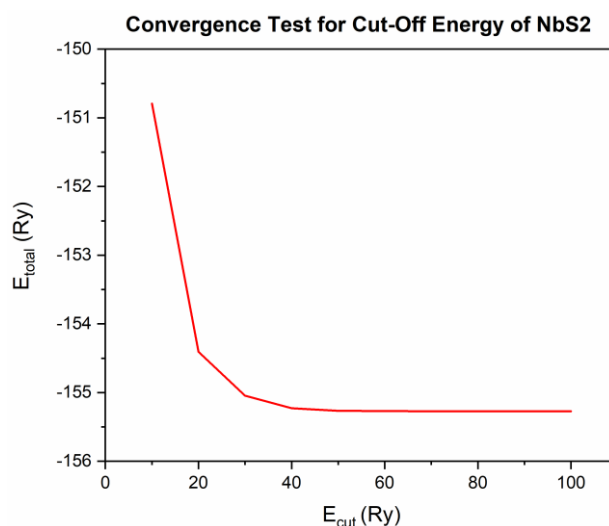


Figure 5.2: Convergence calculation for the cut-off energy of NbS₂

On the other hand, for k-points mesh convergence test, as shown in Fig. 5.3 below, the convergence calculations for k-points grid are done by performing multiple series of calculations for the total energy while varying the number of k-points in the form of $k \times k \times 1$ and fixed the cut-off kinetic energy at 80 Ry. The total energy is then plotted in relation to the k-point number, thus showing a curve that converges towards a constant value. As you can see, the total energy converges after 4 k-point and remain relatively from 6 till 8. Although there's a dip in 5 k-point, the difference is relatively small and insignificant, this was probably due to the discrepancy in computing processes.

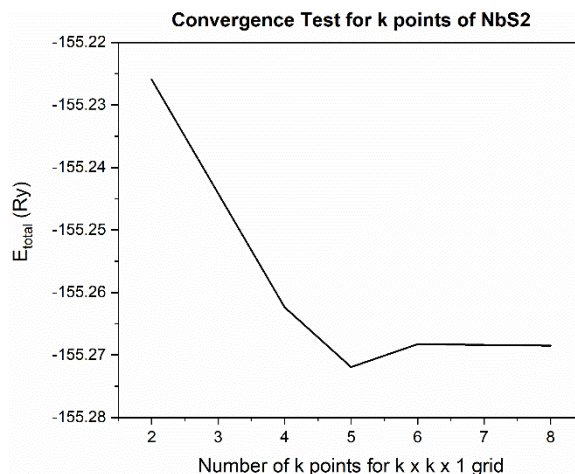


Figure 5.3: Convergence calculation for the k points grid of NbS₂

5.1.2 Band Structure and Density of States

The monolayer structure of 2D NbS₂ with a vertical gap of 18 Å between cells. For the calculation, the cut-off kinetic energy is set to 80 Ry and the k-point mesh is set to 5×5×1. By using VC-relax function in Quantum Espresso, the relaxed data or parameters were obtained. The fermi energy of NbS₂ is obtained to be -0.9513 eV compared to the fermi energy of -0.9077 eV from SCF run.

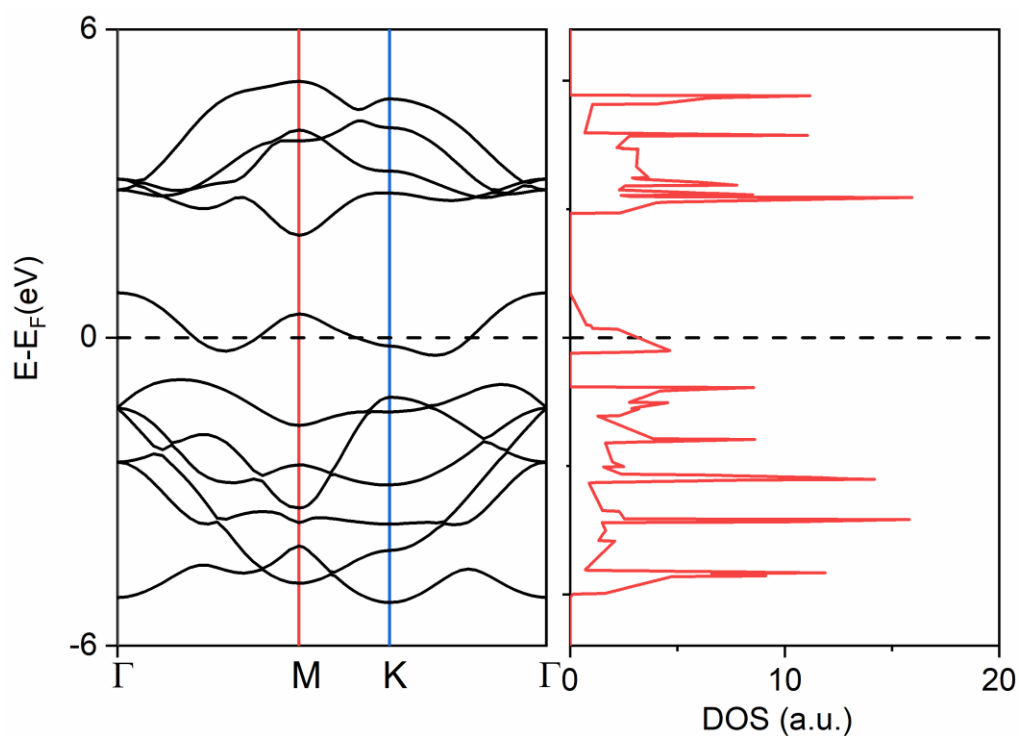


Figure 5.4: The calculated band structure and DOS for NbS₂

5.2 Niobium Diselenide (NbSe₂)

Similar to NbS₂, first and foremost, the three-dimensional crystal structure of NbSe₂ is constructed by having its cell parameters and atomic position input into the NbSe.scf.in file. The material parameter is obtained from the website 2dmatpedia where 2dm-3941 is the material ID for this NbSe₂. This NbSe₂ is a hexagonal 2H-phase polytype and belonging to the space group P-6m2. The pseudopotential files used to perform the calculations are Nb_OCNV_PBE_sr.upf and Se_OCNV_PBE_sr.upf. These pseudopotential codes are optimized norm-conserving Vanderbilt pseudopotential (ONCV PSP or OCNV) scalar-relativistic version produced by D.R. Hamann. The crystal structure is then visualized using XCrySDen as shown in Fig. 5.5 below. From SCF calculation, its fermi energy is -0.2154 eV.

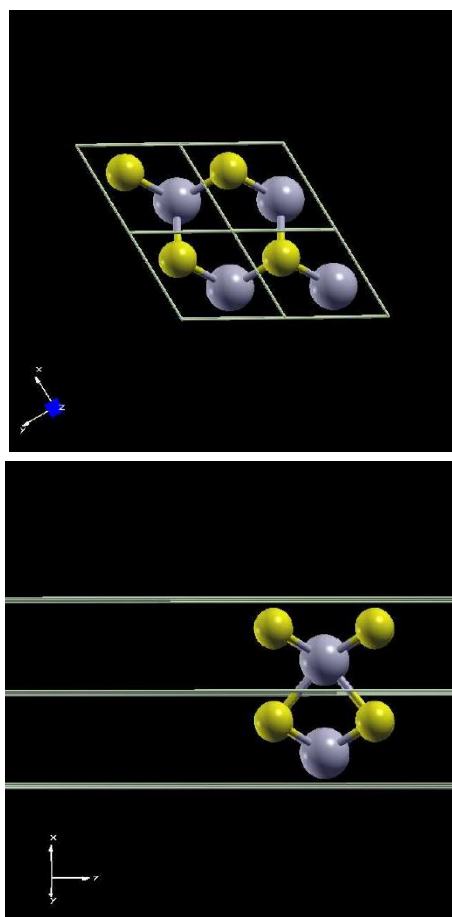


Figure 5.5: Top and Side view of NbSe₂ atomic structure from XCrySDen

5.2.1 Convergence Tests

The optimum cut-off kinetic energy and k-point mesh have to be determined before any band structure calculations can be performed. As shown in Fig. 5.6 below, the convergence calculations for cut-off kinetic energy (E_{cutwfc}) are done by performing multiple series of calculations for the total energy while varying the cut-off kinetic energy input and fixed the k-points mesh at $5 \times 5 \times 1$. The total energy is then plotted in relation to the cut-off kinetic energy, thus showing a curve that converges towards a constant value. As you can see, the total energy converges after 40 Ry point and remain relatively constant through 60Ry to 100 Ry.

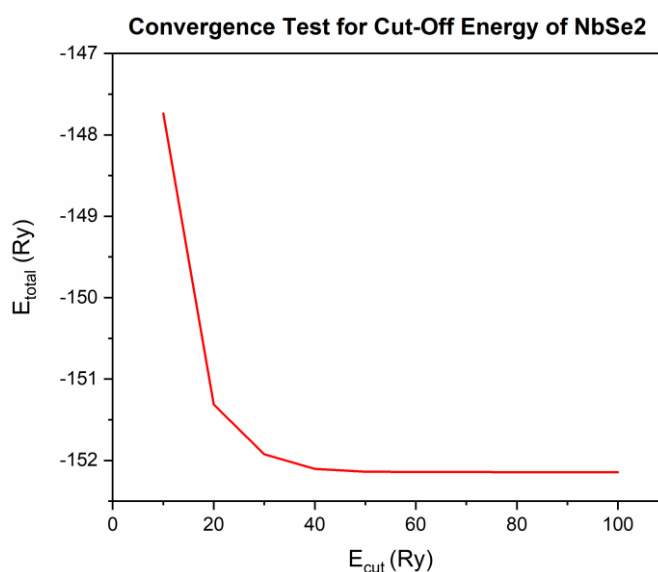


Figure 5.6: Convergence calculation for the cut-off energy of NbSe₂

On the other hand, for k-points mesh convergence test, as shown in Fig. 5.7 below, the convergence calculations for k-points grid are done by performing multiple series of calculations for the total energy while varying the number of k-points in the form of $k \times k \times 1$ and fixed the cut-off kinetic energy at 80 Ry. The total energy is then plotted in relation to the k-point number, thus showing a curve that converges towards a constant value. As you can see, the total energy converges after 4 k-point and remain relatively from 6 till 8. Although

there's a dip in 5 k-point, the difference is relatively small and insignificant, this was probably due to the discrepancy in computing processes.

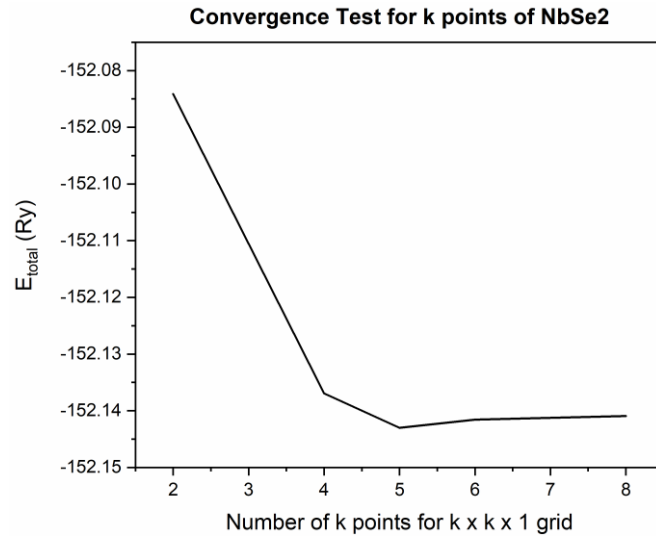


Figure 5.7: Convergence calculation for the k points grid of NbSe₂

5.2.2 Band Structure and Density of States

The monolayer structure of 2D NbSe₂ with a vertical gap of 18 Å between cells. For the calculation, the cut-off kinetic energy is set to 80 Ry and the k-point mesh is set to 5×5×1. By using VC-relax function in Quantum Espresso, the relaxed data or parameters were obtained. The fermi energy of NbS₂ is obtained to be -0.1937 eV compared to the fermi energy of -0.2154 eV from SCF run.

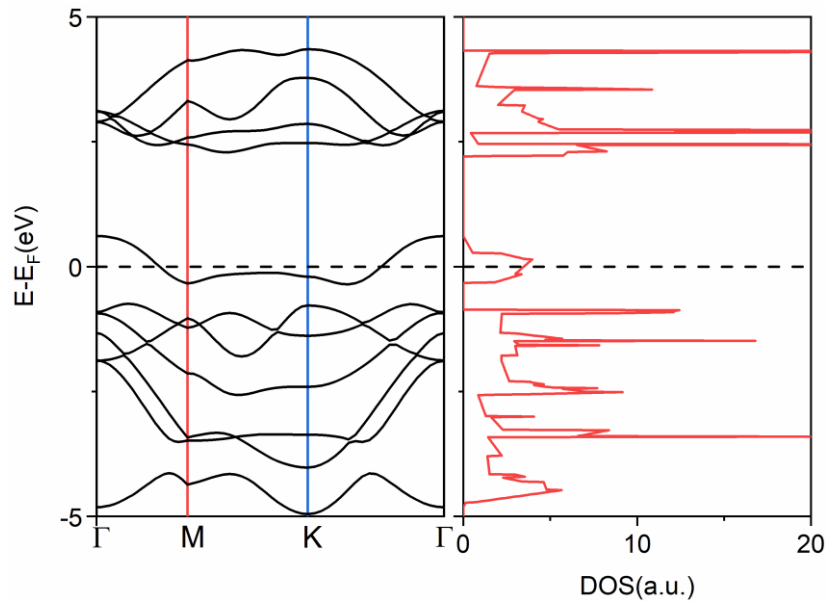


Figure 5.8: The calculated band structure and DOS for NbS₂

5.3 Crystal Structure

The crystal structure of NbS₂ and NbSe₂ produced after optimization are compared with the literature reviewed values that applied similar XC functional with this work in Table 5.1 and Table 5.2 below.

Lattice constant, a (Å)	Source
3.353	From this work
3.355	Zang <i>et al.</i> (2020)
3.321	Tissen <i>et al.</i> (2013)

Table 5.1: Lattice constants of NbS₂ from literature review that applied GGA functional

Lattice constant, a (Å)	Source
3.487	From this work
3.483	Zang <i>et al.</i> (2020)
3.463	Sidoumou <i>et al.</i> (2021)

Table 5.2: Lattice constants of NbSe₂ from literature review that applied GGA functional

As observed, our data are in excellent agreement with the reviewed values in the literature from the theoretical studies.

5.4 Actuator Performance

In Fig. 5.9 and Fig. 5.10 respectively, the actuator strain ε of the NbS_2 and NbSe_2 is shown as a function of charge doping q ranging from -0.12 to 0.12 e/atom.

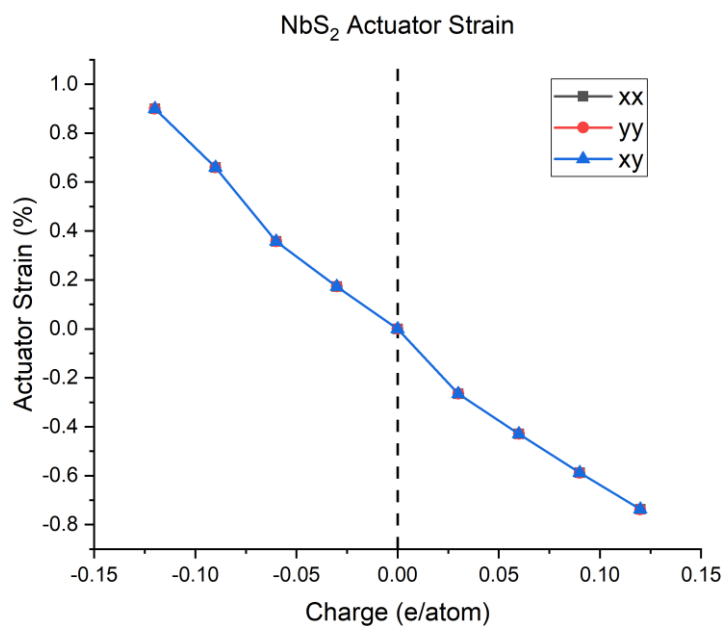


Figure 5.9: Actuator strain of NbS_2 as a function of charge doping ranging from -0.12 to 0.12 e per atom.

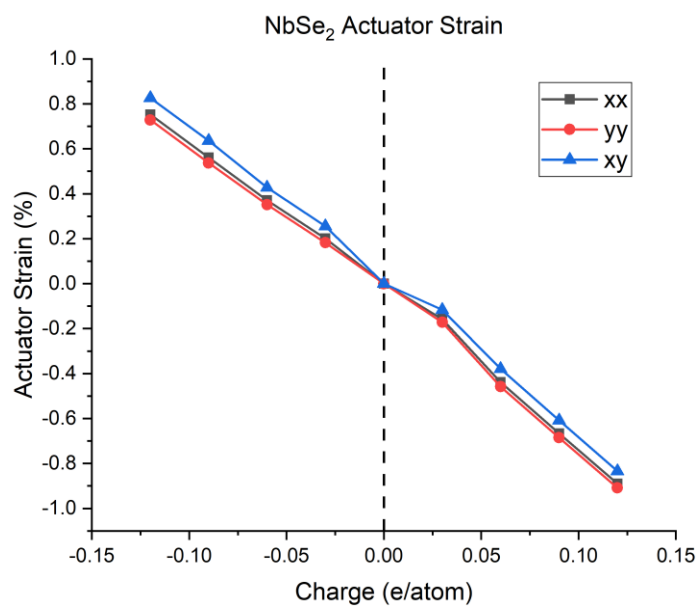


Figure 5.10: Actuator strain of NbSe_2 as a function of charge doping ranging from -0.12 to 0.12 e per atom.

In the neutral doping case ($q = 0$), strain, $\varepsilon = 0$ is obtained. For the electron doping case, ε is approximately a linear function of charge(q). Both materials show isotropic strain under charge doping (Thanh & Hung & Truong, 2018). As observed from the figures above, the ε values are heavily influenced on the number of S and Se. In which under the same charge doping case, NbSe₂ strain value is higher than NbS₂.

5.5 Mechanical Performance

The mechanical properties of NbS₂ and NbSe₂ at neutral charge doping are calculated from Quantum ESPRESSO and obtained in Table 5.3 below.

Materials [N/m]	a_0	C_{11}	C_{22}	C_{12}	Y_{10}	Y_{01}	ν_{10}	ν_{01}
NbS ₂	3.353	137.54	140.94	42.95	124.45	127.53	0.3047	0.3122
NbSe ₂	3.487	97.23	97.68	33.07	86.03	86.43	0.3386	0.3401

Table 5.3: Mechanical properties of neutral charge ($q=0$) NbS₂ and NbSe₂

At the moment of this report writing, the lack of experimentally exfoliated NbS₂ and NbSe₂ monolayer materials have led to issue of verifying our results. There are currently no available open-source data for us to determine the accurate value for the Young's moduli and Poisson ratio obtained from this work. As a result, parameters such as monolayer thickness or buckling height for NbS₂ and NbSe₂ are presumed using assumptions of around 3 Å. The following graphs are just their mechanical properties estimated using other similar materials and it shows very accurate predictions.

Fig. 5.11 and Fig 5.12 below shows the stress-strain curve of NbS_2 and NbSe_2 respectively.

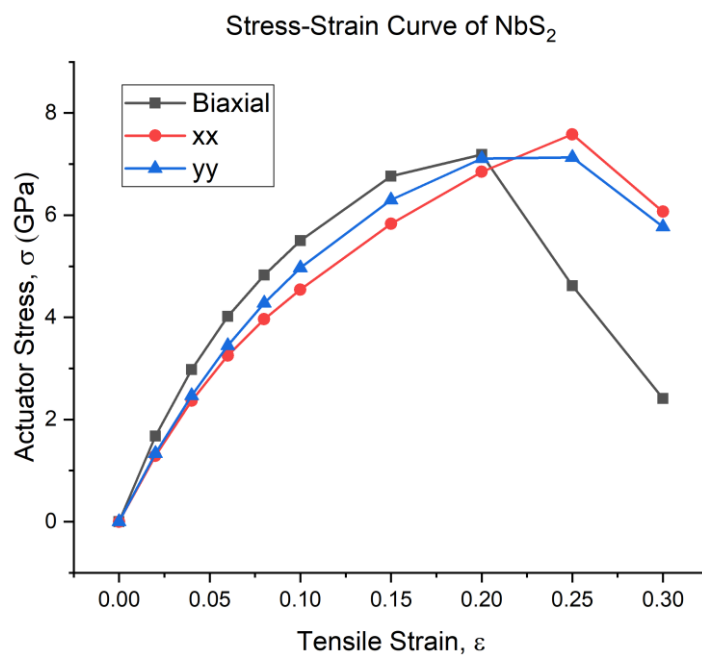


Table 5.11: The stress-strain curve of NbS_2 in biaxial, x and y directions.

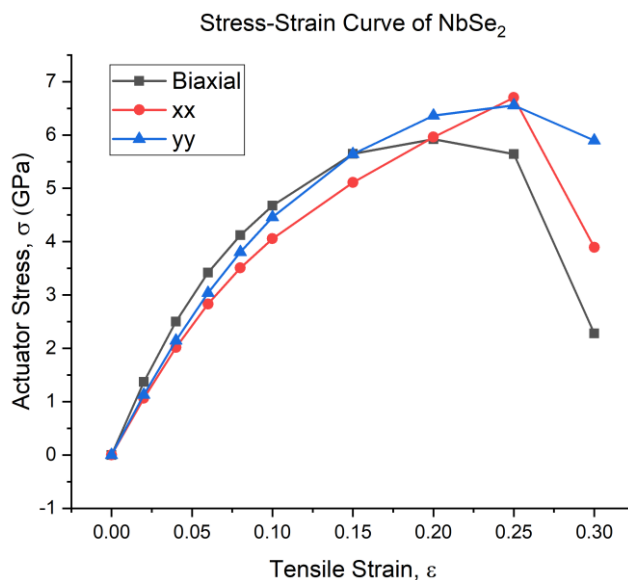


Table 5.12: The stress-strain curve of NbSe_2 in biaxial, x and y directions.

Looking at the stress-strain curves, anisotropic behaviour of these 2D hexagonal material can be observed under tensile strain. The linear elastic limit of NbS_2 is at around $\varepsilon=0.20$ whereas the elastic limit NbSe_2 of is at around $\varepsilon=0.25$. Therefore, it can be concluded that the tensile strength of is NbSe_2 higher than NbS_2 .

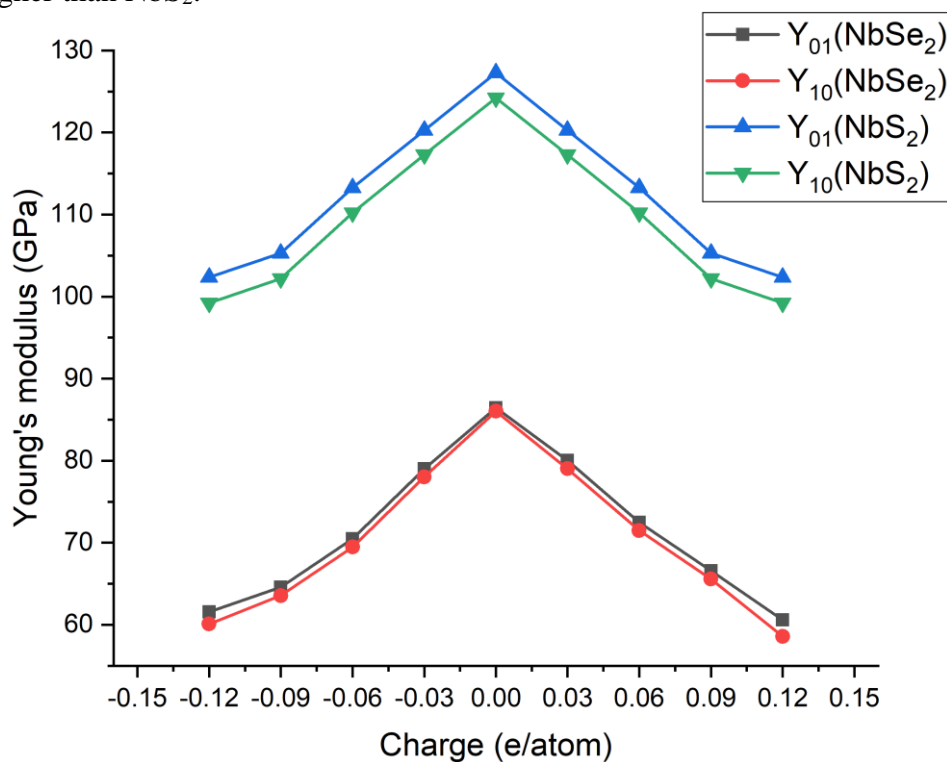


Table 5.13: Young's moduli of NbS_2 and NbSe_2 plotted as function of charge doping per atom

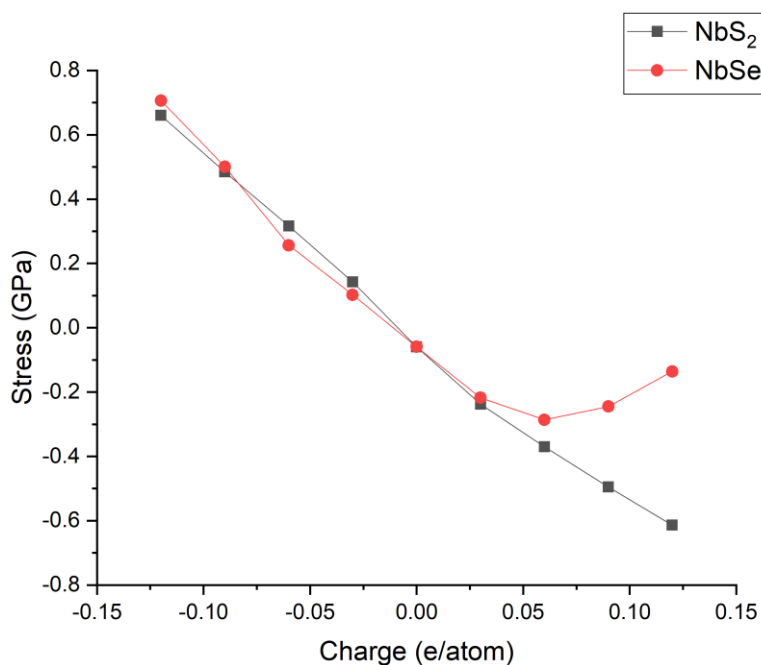


Table 5.14: Stress generated by NbS₂ and NbSe₂ plotted as function of charge doping per atom

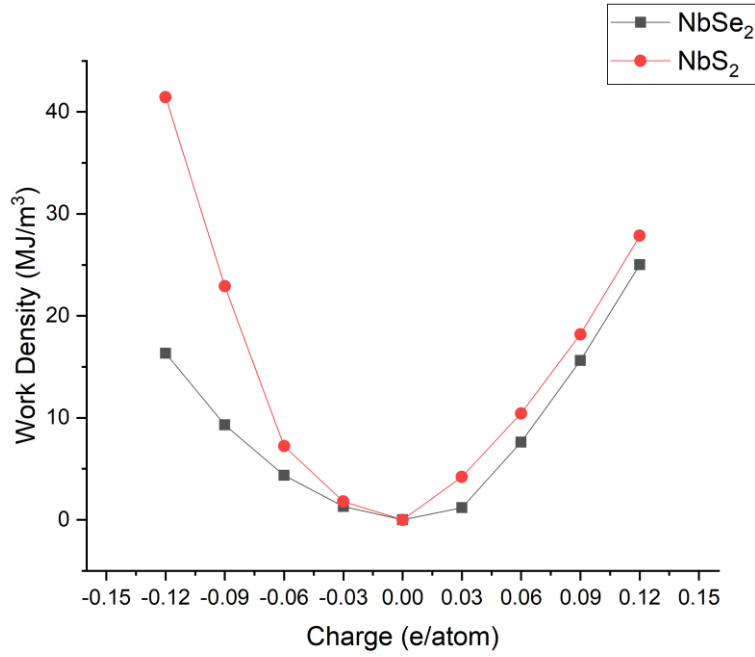


Table 5.15: Work density per cycle of NbS₂ and NbSe₂ plotted as function of charge doping per atom

With the assumption of effective layer thickness of NbS₂ and NbSe₂, the stress generated can determine the power of electromechanical actuators, $\sigma = Y\varepsilon$. The performance of the electrotechnical actuators can then be characterized by the work density per cycle expressed as:

$$W_s = \frac{1}{2} Y \varepsilon^2$$

The highest W_s value obtained in NbS₂ is at $q=-0.12$ e/atom with 41.4 MJ/m³ and in NbSe₂ is at $q=0.12$ e/atom with 25 MJ/m³. These work density per cycle are at least 300 times more than that of mammalian muscle, which is only around 0.08 MJ/m³. These results suggest that electron doping should be excellent to achieve high-performance electromechanical actuator for NbS₂ and NbSe₂ in artificial muscle application.

CHAPTER 6

CONCLUSION AND RECOMMENDATION

6.1 Summary

In summary, we have studied the electromechanical actuator performance of the 2D TMDC materials with 1H structures using first-principle calculations of DFT. The properties of hexagonal H-phase NbS₂ and NbSe₂ are investigated using this framework via Quantum ESPRESSO. We have evaluated the charge induced actuation performance of NbS₂ and NbSe₂ by studying their structural properties and electromechanical properties. The lattice structure constants of NbS₂ and NbSe₂ agrees with the results obtained from literature review.

With charge doping per atom ranging from +0.12 e/atom to -0.12 e/atom, linear and isotropic characteristics have been observed from the strain of NbS₂ and NbSe₂. The Young's modulus and Poisson's ratio obtained from this work are in excellent agreement with published values. Unfortunately, these values cannot be verified for their accuracy due to the absence of experimentally proven data or open and available data sources. The electromechanical actuator performance of the NbS₂ and NbSe₂ is highly dependent on the charge doping level. The NbS₂ and NbSe₂ have the best electromechanical performances when doped with electron with work density per cycle as high as 41.4 MJ/m³ and 25 MJ/m³, respectively. These results of this first-principle study show promising information for designing and fabricating artificial muscles with NbS₂ and NbSe₂.

6.2 Recommendation for Future Works

It is in our best interest to increase the accuracy of the results obtained from the DFT calculation via Quantum ESPRESSO. Therefore, we recommend that higher k-point grid value can be implement on the same materials when future studies are conducted instead of using lower value such as 5 × 5 × 1 like in this work.

6.3 Problems Encountered

There are slight discrepancies between the results calculated using Quantum Espresso in different PC. With the same lines of codes and files used, the calculated output of scf, bands, and DOS might defer slightly based on the central processing unit (CPU) model of that particular computer. For example, when performing calculation with my personal desktop PC with the CPU model Ryzen 5 3600, the fermi energy of NbS₂ is -0.9077 eV whereas if the calculations are performed on my HP Z230 workstation, the fermi energy is -0.9076 eV. Although the difference is extremely small, we cannot simply ignore the fact that different computing unit may cause a tiny disparity between results. We might not know whether this slight inconsistency would result in larger errors from the results obtained in future calculations.

6.4 Recommended Solutions

In order to maintain consistency of the results obtained, it is recommended that all calculations done using Quantum Espresso has to be performed on the same computer.

REFERENCES

- Akbari, E., Jahanbin, K., Afroozeh, A., Yupapin, P. and Buntat, Z., 2018. Brief review of monolayer molybdenum disulfide application in gas sensor. *Physica B: Condensed Matter*, 545, pp.510-518.
- Akinwande, D., Brennan, C., Bunch, J., Egberts, P., Felts, J., Gao, H., Huang, R., Kim, J., Li, T., Li, Y., Liechti, K., Lu, N., Park, H., Reed, E., Wang, P., Yakobson, B., Zhang, T., Zhang, Y., Zhou, Y. and Zhu, Y., 2017. A review on mechanics and mechanical properties of 2D materials—Graphene and beyond. *Extreme Mechanics Letters*, 13, pp.42-77.
- Andreeva, Daria V. 2020. Introduction To Two-Dimensional Materials. *Surface Review and Letters*, 28, 2140005-. doi: 10.1142/S0218625X21400059
- B. Morosin, - Structure refinement on NbS₂, *Acta Cryst.* (1974), Vol. B30, p. 551-552.
- Bilbao crystallographic server. <http://www.cryst.ehu.es/>. Accessed: 2018-05-08
- Dai, Z., Liu, L. and Zhang, Z., 2019. Strain Engineering of 2D Materials: Issues and Opportunities at the Interface. *Advanced Materials*, p.1805417.
- D.R. Powell and R.A. Jacobson, - The crystal structure of 3-R Nb_{1.06}S₂, *J. Solid State Chem.* (1981), Vol. 37, p. 140-143.
- Doran, N.J. & Titterington, D & Riccò, Bruno & Wexler, G. (2001). A tight binding fit to the bandstructure of 2H-NbSe₂ and NbS₂. *Journal of Physics C: Solid State Physics*. 11. 685. 10.1088/0022-3719/11/4/012.
- F. Jellinek, G. Brauer, H. Müller, - Molybdenum and Niobium Sulphides, *Nature* (1960), Vol.185, p. 376-377.
- F. Kadijk and F. Jellinek, - The system niobium-sulphur, *J. Less-Common Met.* (1969), Vol. 19, p. 421-430.
- Garay-Tapia, A., Romero, A. and Barone, V., 2012. Lithium Adsorption on Graphene: From Isolated Adatoms to Metallic Sheets. *Journal of Chemical Theory and Computation*, 8(3), pp.1064-1071.
- Geim, A.K. and Grigorieva, I.V., 2013. ‘Van der Waals heterostructures’, *Nature*, 499(7459), pp. 419–425.
- Giannozzi, P., Andreussi, O., Brumme, T., Bunau, O., Nardelli, M.B., Calandra, M., Car, R., Cavazzoni, C., Ceresoli, D., Cococcioni, M. and Colonna,

- N., 2017. Advanced capabilities for materials modelling with Quantum ESPRESSO. *Journal of Physics: Condensed Matter*, 29(46), p.465901.
- Giannozzi, P., Baroni, S., Bonini, N., Calandra, M., Car, R., Cavazzoni, C., Ceresoli, D., Chiarotti, G.L., Cococcioni, M., Dabo, I. and Dal Corso, A., 2009. QUANTUM ESPRESSO: a modular and open-source software project for quantum simulations of materials. *Journal of physics: Condensed matter*, 21(39), p.395502.
- Haynes, William M., ed. (2011). *CRC Handbook of Chemistry and Physics* (92nd ed.). Boca Raton, FL: CRC Press. p. 4.78. ISBN 1-4398-5511-0.
- Kim, J. & Lee, Z. (2018). Phase Transformation of Two-Dimensional Transition Metal Dichalcogenides. *Applied Microscopy*. 48. 43-48. 10.9729/AM.2018.48.2.43.
- Lide, D. R., ed. (2005). *CRC Handbook of Chemistry and Physics* (86th ed.). Boca Raton (FL): CRC Press. p. 4.76. ISBN 0-8493-0486-5.
- Madden J D W, Vandesteeg N A, Anquetil P A, Madden P G A, Takshi A, Pytel R Z, Lafontaine S R, Wieringa P A and Hunter I W 2004 *IEEE J. Ocean. Eng.* 29 706–28
- Si, J., Zheng, Q., Chen, H., Lei, C., Suo, Y., Yang, B., ... Ostrikov, K. (Ken). 2019. Scalable Production of Few-layer Niobium Disulfide Nanosheets via Electrochemical Exfoliation for Energy - Efficient Hydrogen Evolution Reaction. *ACS Applied Materials & Interfaces*. doi:10.1021/acsami.8b22052
- Sidoumou M, Merazka S, Gómez-Herrero A, Kars M, Thierry R. 2021. X-ray diffraction and theoretical study of the transition 2H-3R polytypes in $\text{Nb}_{1+x}\text{Se}_2$ ($0 < x < 0.1$) *PeerJ Inorganic Chemistry* 3:e2 <https://doi.org/10.7717/peerj-ichem.2>
- Tissen, V. & Osorio, M. & Brison, J. & Nemes, Norbert & Gaarcia, Mar & Cario, Laurent & Rodière, Pierre & Vieira, Sebastian & Suderow, H.. (2013). Pressure dependence of superconducting critical temperature and upper critical field of 2H-NbS₂. *Physical Review B*. 87. 10.1103/PhysRevB.87.134502.
- Thanh, Vuong & Hung, Nguyen & Truong, Do. (2018). Charge-induced electromechanical actuation of Mo- and W-dichalcogenide monolayers. *RSC Advances*. 8. 38667-38672. 10.1039/C8RA08248K.
- Zang, Yanmei & Ma, Yandong & Peng, Rui & Wang, Hao & Huang, Baibiao & Dai, Ying. (2020). Large valley-polarized state in single-layer NbX₂

(X = S, Se): Theoretical prediction. Nano Research. 14.
10.1007/s12274-020-3121-1.